DISSERTATION

Superconducting flux qubits with π-junctions

Supraleitende Flussqubits mit π-Kontakten

Anastasia Shcherbakova

zur Erlangung des akademischen Grades
DOKTOR DER NATURWISSENSCHAFTEN
der Fakultät für Physik
des Karlsruher Instituts für Technologie (KIT)
Genehmigte Version

Tag der mündlichen Prüfung: 16. Mai 2014

Referent	: Prof. Dr. A. Ustinov
Korreferent	: Prof. Dr. G. Weiss

14. Juli 2014

Autor
Anastasia Shcherbakova

Kontakt
anastasia.shcherbakova@kit.edu

Contents

1 Introduction

Personal view

Since I heard about quantum physics during the first semester of my university studies I was both intrigued and charmed. Rumors about "the electron which can interfere with itself while passing through two holes" and "wave functions which "feel" each other in spite of the barrier" caught my imagination and inflamed me with interest. Probably, it was just the childish wish of wonder, but this fascination played a good trick on me. When I was suggested to work in the area of superconductivity, and later - superconducting flux quantum bits, I agreed without doubting. And then the story began.

My experience of superconducting quantum bits started with the fabrication of flux qubits and took the main part (about 65 %) of my time. Sub-micron rings interrupted with 3 Josephson junctions can be easily drawn on the paper but need quite a number of exact parameters being adjusted during fabrication steps such as spin-coating, lithography, developing, argon cleaning, two-angle shadow evaporation, lift off and other techniques. Then the second layer of abstraction comes. In this aluminum ring, after it becomes superconducting, and in the presence of the external magnetic field, which is quantized in the loop, two currents appear. These currents flow in opposite directions and exist simultaneously but have different proba-

bility of presence. I remember how we argued until we lost our voices - are they blinking or just flowing one through another smoothly? But this is quantum mechanics, could we imagine it at all with an everyday experience based on our imperfect senses?

Now, moving towards the more theoretical introduction, in flux qubits we have a double-well potential (how it appears will be discussed in Chap. 2). The system has two stable states at the bottom of these energy wells which are associated with the positive and negative persistent currents circulating in the loop and named persistent current states. Due to the tunneling through the barrier, which separates the two potential minima, the persistent current states form a symmetrical and anti-symmetrical superposition with an energy gap Δ. The superpositions mentioned above are named ground $|\mathrm{g}\rangle$ and excited $|\mathrm{e}\rangle$ states of a flux qubit. And then the last level of abstraction comes: while a state of an ordinary bit is either "0" or "1", a qubit can be in an arbitrary superposition $a|0\rangle + b|1\rangle$, where $|0\rangle$ and $|1\rangle$ are referred to the ground and excited flux qubit states, respectively, and a and b are complex numbers. This opens breathtaking possibilities of information encoding!

There are a lot of possibilities to realize qubits. For example, photons [1], electron spins [2], nuclear spins [3], trapped ions [4] or NV centers in diamonds (nitrogen-vacancy centers) [5] could be operated as qubits in experiments. However, the most promising concept nowadays to create qubits for quantum computation is based on electrical circuits made of superconducting materials. In contrast to other approaches, they are scalable and their parameters are easy to control.

Now let us consider the scientific motivation of this thesis.

Scientific motivation

My exact task was to fabricate and measure hybrid Nb/Al flux qubits with SFS π-junctions - $Nb/Cu_{0.47}Ni_{0.53}/Nb$ trilayers with magnetic properties.

Two-angle evaporation process has been successfully used for a variety of superconducting qubit types [6, 7] (charge, flux, transmon, fluxonium, etc.) and appears to be most suitable for obtaining well-defined sub-micron $Al/AlO_x/Al$ Josephson junctions with reliable characteristics and low density of microscopic two-level defects in the oxide tunnel barrier [8, 9].

While niobium serves as the base material for most of conventional superconducting circuits employing $Nb/AlO_x/Nb$ Josephson junctions, quantum coherence times of Nb-based qubits [10, 11, 12] are significantly shorter than those of their Al-based counterparts. Aluminum superconducting flux qubits can be made very compact, while well-controlled sizes of Josephson junctions insured by two-angle evaporation make it possible engineering qubit potential with precisely defined parameters [13].

The magnetic bias used to drive the flux qubit to its working point is a source of significant noise, leading to dephasing. The flux qubit has the most favorable operation point of minimal dephasing corresponding to the magnetic flux threading its loop of about $\Phi_0/2$, where Φ_0 is the magnetic flux quantum. In order to reduce the effects of external magnetic noise, it was proposed to avoid magnetic biasing by using the so-called π-junction in the qubit loop [14, 15]. The most reliable and well-established process of implementing π-junctions relies on Nb-based technology of superconductor-ferromagnet-superconductor (SFS) Josephson junctions [16]. The conventional fabrication process

of π-junctions is based on the depositing of an SFS Nb/CuNi/Nb trilayer, forming the junction, followed by depositing the upper Nb wiring [16]. A π-junction in the superconducting loop having large enough critical current acts as a phase battery which biases the loop such that the phase shift on the junction is π [17]. The effect of such a phase shifter is equivalent to applying flux of $\Phi_0/2$ through the loop [17, 18]. SFS phase shifters have been already successfully implemented in Nb-based phase qubit circuits [19], but not yet used with flux qubits.

A complication arising along this development is due to two completely separated and not compatible technological steps, first one for making relatively large SFS Nb/CuNi/Nb junctions, followed by another process of manufacturing more fragile sub-micron Al/AlO_x/Al junctions needed for highly-coherent flux qubits. Aluminum two-angle evaporation is done in a separate setup, and pre-fabricated Nb structure is exposed to air under which natural oxide NbO_x is formed on Nb surface. This complication makes the implementation of the SFS π-junction in the Al flux qubit loop challenging and requires removing the NbO_x completely before the deposition of Al part of the flux qubit.

In this thesis, we present a fabrication and current-voltage measurements of Al/AlO_x/Al Josephson junctions deposited on Nb pads. Before deposition of Al, the unwanted NbO_x on the surface of Nb is etched down in-situ by using the Ar directed beam. The described technology gives a possibility of combining a variety of Nb-based superconducting circuits, like π-junction phase-shifters [19], with sub-micron Al/AlO_x/Al junctions fabricated with the help of the standard double-angle evaporation technique. Using this approach, we fabricated hybrid Nb/Al flux qubits with and without the SFS π-junctions.

For characterization of qubits, we employ the readout for flux qubits by measuring a dispersive shift of a $\lambda/4$ resonator coupled to the qubit. We study dispersive magnetic field response of these qubits as well as their spectroscopy characteristic.

Thesis outlook

The operation regime of flux qubits and basics of the theory of π-junctions are summarized in the second chapter. This chapter would be useful for an unprepared reader in order to understand the logic of the experiment.

In the third chapter, the fabrication procedure developed for obtaining electronically transparent contact between Nb and Al parts of the Al/Nb hybrid flux qubit circuits is explained. The necessary fabrication steps and lists of optimized process parameters are included so that one could use it later as a help for his own challenges.

At last, the measurement setups and measurements which confirm qubit behavior in the fabricated samples and the obtained results are presented in the forth and discussed in the fifth chapters. The spectroscopy plots and the method to distinguish a flux qubit with a π-junction from a flux qubit without a π-junction are also discussed.

2 Superconducting qubits and π-junctions

This chapter reviews the basics of superconductivity and Josephson effects, because in order to understand the behavior of a hybrid flux qubit with a π-junction, we have to analyze its elements.

Energy spectrum and dynamics of a flux qubit under an external microwave drive will also be discussed, as well as sources of decoherence. Interaction of a flux qubit with a resonator will be considered from the quantum point of view, explaining underlying principles of a dispersive readout measurement scheme. Finally, a short insight in the nature of ferromagnetic materials will help us to understand a π-junction working principle, which will be the last building block of our system.

2.1 Superconductivity and Josephson effect

2.1.1 Superconductivity

In the year 1911 in Leiden laboratory, Holland, Kammerling-Onnes found out that the resistance of mercury drops dramatically under a temperature of about 4 K and stays undetectable down to the possible reachable temperatures [20]. Now we

know, that the resistance is not noticeable down to the value of 10^{-24} Ohm·cm. For comparison, the specific resistance of pure copper is about 10^{-9} Ohm·cm. The phenomenon was named as superconductivity, the materials which showed such a behavior - superconductors, and the temperature under which the superconducting state is detected - a critical temperature. Every superconductor has its own critical temperature, for niobium (Nb) it is around 9 K, for aluminum (Al) it is approximately 1.2 K.

In 1926 Albert Einstein posed a remarkable question [21]:

" Of particular interest is the question whether a link between two superconductors also turns superconducting."

Then it was investigated in details in 1962 by Brian Josephson [22, 23] and experimentally proved in 1963 by P. Anderson and J. Rowell that superconductivity is a quantum phenomena [24]. The experiment was performed on two superconducting materials, tin (Sn) and lead (Pb), interrupted by a weak link, originally a thin layer of insulating oxide. It was found out, that the current lower than some critical value I_c can flow through this system without any dissipation. The explanation is based on the fact, that the superconducting state of a metal is the state where electrons form a Bose-condensate and are described by a common wave function, called the superconducting order parameter:

$$\Psi_i = \Psi_0 \exp^{i\Theta_i}, \tag{2.1}$$

where Θ_i is the phase of a wave function of superconducting electrons, and Ψ_0 is its amplitude.

If we consider two superconducting materials and connect them through a weak link, for certain parameter of weakness we can obtain an overlap of the wave functions of electrons.

The density of the superconducting current, which flows due to this effect, is determined by a phase gradient ψ on the junction:

$$\psi = \Theta_1 - \Theta_2, \tag{2.2}$$

where Θ_1 is the phase of the order parameter of the first material, and Θ_2 of the second one.

2.1.2 Josephson effects

Brian Josephson in [22, 23] wrote that the superconducting current in the tunnel junction described above can be expressed by

$$I = I_c \sin \psi, \tag{2.3}$$

where I_c is the maximum of a non-dissipative current, named the critical current. The expression (2.3) is called the first Josephson equation. If the current through the junction exceeds I_c, we obtain a voltage drop across the junction and the Josephson generation according to the second Josephson equation:

$$2eV = \hbar \frac{\partial \psi}{\partial t}, \tag{2.4}$$

where e is the electron charge, V is the drop of the voltage across the Josephson junction, $\hbar$ is the Plank constant. If we consider the energy which is stored in the junction, using (2.3) and (2.4) from

$$E = \int_0^t IV dt \tag{2.5}$$

we will get

$$E = E_J(1 - \cos \psi) \tag{2.6}$$

where

$$E_J = \hbar I_c/2e = \Phi_0 I_c/2\pi \tag{2.7}$$

is the Josephson energy - the maximum value of the junction energy reduction due to the weak link between the superconducting materials. Here $\Phi_0 = h/2e$ is the magnetic flux quantum. In fact, a Josephson junction is a non-linear inductance which stores energy during the change of the current through it.

There are a lot of types of structures with weak links - nanobridges, point contacts and tunnel junctions. The tunnel junctions can consist of superconductors with a variety of number and type of materials in between. In this thesis we will focus on Al/AlO_x/Al Josephson junctions. AlO_x can be naturally formed on the Al surface and then covered by the second Al layer during the same evaporation process without breaking up the setup vacuum. This gives the opportunity to obtain high quality Josephson junctions with reproducible current-voltage characteristics, having a minimum number of fabrication steps: spin-coating, lithography, evaporation and lift off. Therefore this kind of junctions is very attractive for building of quantum integrated circuits on the base of superconducting quantum bits. The example of an Al Josephson junction is depicted in Fig. 2.1.

2.1.3 RCSJ model of a Josephson junction

The Josephson junction can be modeled by the equivalent electrical circuit which includes a parallel combination of a resistance, a capacitance and a non-linear Josephson element, illustrated in Fig. 2.2.

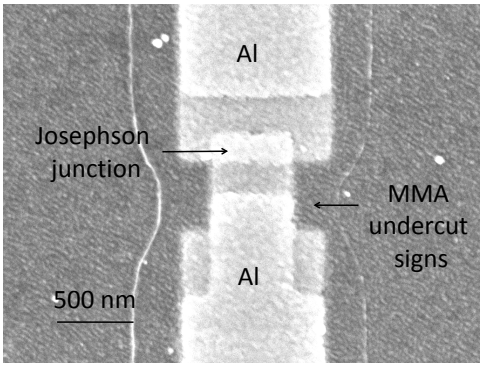

Figure 2.1: SEM picture of an Al/AlO_x/Al Josephson junction.

The resistive part represents the shunting resistance of the junction, the Josephson element behaves according to the equation (2.3) and the capacitance C is defined by the capacitance of the overlapping electrodes of the tunnel junction. Besides the Josephson energy (2.7) we should also take into account the charging energy of the junction:

$$E_C = \frac{e^2}{2C} \tag{2.8}$$

where e is the charge of the electron [25].

2.2 Flux quantization

In the year 1933 Meissner and Ochsenfeld [26] published the results on their experiments about superconductors in a magnetic field. They observed that the magnetic field in a bulk superconductor remains always equal to zero and doesn't depend on

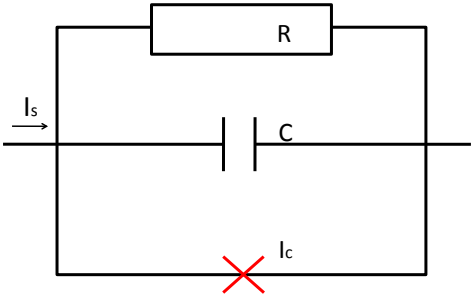

Figure 2.2: Equivalent circuit model of a Josephson junction. The cross marks the non-linear Josephson element, R and C represent the inner resistance and capacitance of the junction.

switching on the magnetic field before or after crossing of the critical temperature point. We will use this statement in order to explain flux quantization. At the moment the penetration depth of the superconductor, mixed state and vortexes will be neglected.

Let us consider a closed cylinder-like hole in a superconductor (see Fig. 2.3). Let us now put it into the magnetic field and cool it down to the critical temperature so that the normal metal-superconductor transition occurs. Now the magnetic field will be displaced from the body of the superconductor and some frozen magnetic flux remains in the hole.

Now we introduce a contour Y which is situated inside the superconductor around the hole as it is depicted in Fig. 2.3 on the distance much larger then the screening length λ.

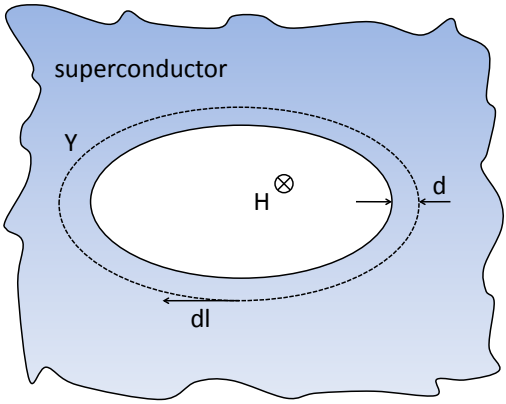

Figure 2.3: A cylindrical hole in the superconductor. The path Y goes in the superconductor material on the distance much larger than the screening length.

For the path integral around the hole we can obtain an expression using the generalized equation of F. London [20]:

$$\frac{h}{2e}\oint_Y \bigtriangledown\theta dl = \oint_Y Adl, \tag{2.9}$$

where A is the vector potential, θ is the phase difference of the wave function around the contour Y, and l is the length of the path. Taking into account that $\oint_Y Adl = \Phi$ we can derive

$$\Phi = (\Phi_0/2\pi)\oint_Y \bigtriangledown\theta dl. \tag{2.10}$$

The wave function (2.1) should be univocal, that is why the last integral should be equal to $2\pi n$, and finally we get

$$\Phi = n\Phi_0, \tag{2.11}$$

what means that the magnetic flux in a hole in the superconductor is quantized.

2.3 Flux qubit

2.3.1 Requirements to quantum bits

In the modern world the concept of a bit in computing and digital communication is well-known: the bit is a minimal unity of the information which can take only one of the two possible values, named "0" and "1". These values can be realized through the two distinct voltage or current levels, two directions of magnetization or polarization, two distinct intensities of light, etc. For bit representation mostly flip-flop circuits are used nowadays.

Another approach of handling the information is quantum computing, based on quantum bits or qubits. Qubit can exist not only in "0" and "1" state, but also in any linear superposition of these two state. Theoretically, quantum circuits could allow to code an enormous quantity of information in comparison to flip-flop ones, but there are several important requirement which should be fulfilled. Di Vincenzo formulated them in 2000 [27]:

1. A scalable physical system with well characterized qubits.
2. The ability to initialize the state of the qubits to a simple fiducial state.
3. Long relevant decoherence times, much longer than the gate operation time.
4. A "universal" set of quantum gates.
5. A qubit-specific measurement capability.

In other words, the qubit has to be addressed, controlled, measured, coupled to its neighbors, and decoupled from the environment.

In case of our work, where we consider the aluminum superconducting flux qubit, the electron beam lithography provides a big flexibility in designs and scaling. The eigenstates of a 3 Josephson junction flux qubit loop are the circulating currents of the opposite signs, called persistent current states (PC states). The physics of flux qubits fulfill all functional criteria for a quantum bit [25]:

1. The superconducting circuit is operated at a sufficiently low temperature so that the PC states can be prepared in their ground state.

2. The PC states can be manipulated precisely with magnetic fields.

3. Two qubits can be coupled inductively, and the inductive coupling can be turned on and off.

4. The PC states can be successfully measured with several types of the readout: SQUID, dispersive and fluxon [28] readouts, for example.

5. The magnetic coupling to the PC states can be made sufficiently weak.

6. As the persistent current flux qubits also have considerably long coherence times, they are promising objects for investigations.

2.3.2 Energy potential and energy levels of a flux qubit. Quantum mechanical description.

The basic flux qubit design contains a ring, interrupted by three Josephson junctions, one is geometrically α times smaller, than

other two, named further large Josephson junctions. The schematic view and micrograph of a flux qubit are depicted in Fig. 2.4.

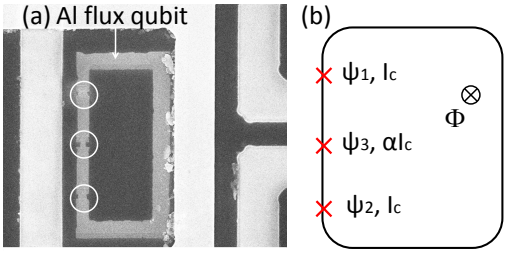

Figure 2.4: a) Aluminum flux qubit: a superconducting aluminum ring is interrupted by three Josephson junctions, marked by circles. The qubit is placed in the fluxon readout environment. b)The schematic representation of a flux qubit with three Josephson junctions.

In this work we will consider flux qubits which have geometrical inductance of the qubit loop much less, than the Josephson inductance of junctions, interrupting the loop, and working in the superconducting limit, what means that

$$E_C \ll E_J. \tag{2.12}$$

The details of different regimes are given in [25]. One of the Josephson junctions has α times smaller area then the other two.

The kinetic energy of the system (with neglecting of the loop capacitance to the ground) can be described by taking into account the capacitance of Josephson junctions:

$$T = 1/2 \sum_{(j)} C_j V_j^2, \tag{2.13}$$

where j=1,2,3 denotes indexes of three Josephson junctions, C_j is the capacitance of the appropriate junction, and V_j is the voltage drop across each junction. According to (2.4) we can rewrite the equation in terms of phase derivatives across the junctions:

$$T = \frac{1}{2}(\frac{\Phi_0}{2\pi})^2 \sum_{(j)} C_j \dot{\psi}^2, \tag{2.14}$$

For the potential energy term we can now write an expression containing the energy of the qubit using (2.7) for all three junctions and the condition of the external flux quantization in the ring [29]:

$$\Sigma\psi_j + 2\pi f = 2\pi N \tag{2.15}$$

where N is the number of flux quanta in the flux loop, ψ_j is the phase difference across the Josephson junction j, j = 1,2,3, and $f = \Phi/\Phi_0 - \frac{1}{2}$ is the flux frustration in the loop relative to $\frac{1}{2}$. In case N=0 we obtain the potential energy profile [25]:

$$U = E_J(2 + \alpha - 2\cos(\frac{\psi_1 + \psi_2}{2})\cos(\frac{\psi_1 - \psi_2}{2}) - \\ -\alpha\cos(2\pi f + 2\frac{\psi_1 + \psi_2}{2})) \tag{2.16}$$

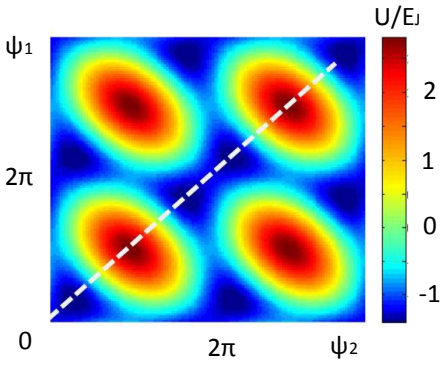

Figure 2.5: The flux qubit periodic energy potential. The dashed line marks a crossection with a doble-well profile.

Plotting U normalized to E_J in the phase space we obtain a two-dimensional periodic pattern with double-well potential unit cell, shown in Fig. 2.5.

The system has two stable states at the bottom of these energy wells which are associated with the positive and negative persistent currents circulating in the loop and named persistent current states. Due to the tunneling through the barrier, which separates the two potential minima, the persistent current states form a symmetrical and anti-symmetrical superposition with an energy gap Δ. The superpositions mentioned above are named ground $|g\rangle$ and excited $|e\rangle$ flux qubit states (see Fig. 2.6). Thoroughly one can calculate them using the quantum mechanical description of the system.

Aiming that, the classically conjugated variables in the classical Hamiltonian are substituted by quantum-mechanical operators, and the coordinate system is rotated to $\psi_p = (\psi_1 + \psi_2)/2$

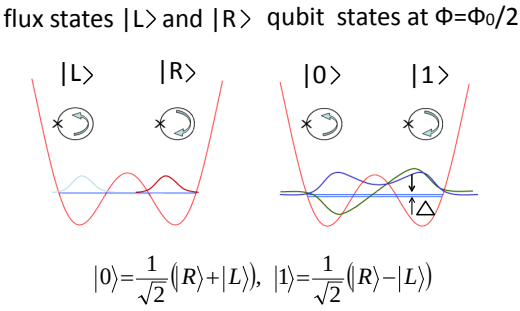

Figure 2.6: Sketch of persistent-current and qubit eigenstates of the flux qubit in the double-well profile at the zero-frustration point.

and $\psi_m = (\psi_1 - \psi_2)/2$. The resulting Hamiltonian is presented in [25] and looks like

$$H_t = \frac{1}{2}\frac{P_p^2}{M_p^2} + \frac{1}{2}\frac{P_m^2}{M_m^2} + E_J(2 + \alpha - 2\cos(\psi_p)\cos(\psi_m) - \\ -\alpha\cos(2\pi f + 2\psi_p)) \quad (2.17)$$

where the momentum operator can be written as $\mathrm{P}_p = -\hbar\partial/\partial\psi_p$ and $\mathrm{P}_m = -i\hbar\partial/\partial\psi_m$ in the phase space, C is the capacitance of the large Josephson junction, mass terms are described as $\mathrm{M}_p = (\Phi_0/2\pi)^2/2\mathrm{C}$ and $\mathrm{M}_m = (\Phi_0/2\pi)^2/2\mathrm{C}(1+2\alpha)$.

Further, the Hamiltonian can be diagonalized numerically on the discrete grid in the phase space and eigenvalues and eigen-wave-functions can be found. The results of the calculation are shown in Figs. 2.7 and 2.8.

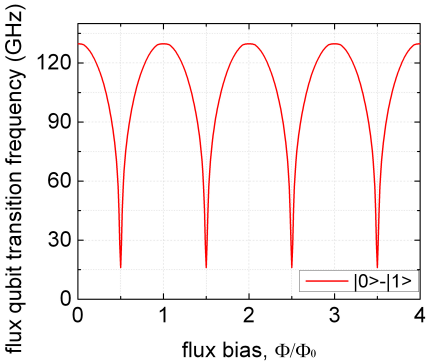

Figure 2.7: Periodical dependence of the flux qubit transition frequencies E_1 - E_0, for the first energy level versus external flux bias current, four periods are shown. The model qubit parameters are $\alpha = 0.59$, $E_c/E_J = 0.0088$, corresponding to $I_c = 1$ μA and are later used for fitting of flux qubit spectroscopy plots.

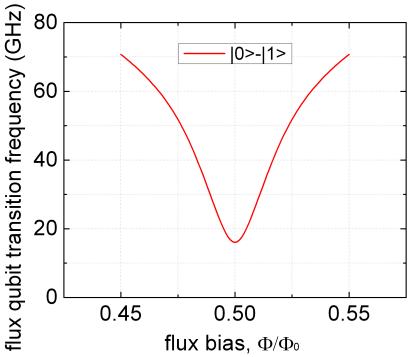

Figure 2.8: Flux qubit transition frequencies E_i - E_0, for the first flux qubit energy level near the $\Phi_0/2$ symmetry point versus external flux bias current. The model qubit parameters are $\alpha = 0.59$, $E_c/E_J = 0.0088$, corresponding to $I_c = 1$ μA. The qubit gap Δ is estimated to be about 14.54 GHz.

The plotted curves represent the energy needed to excite the qubit from the ground state to the first excited state. We can see, that the pattern is Φ_0 periodic. In Fig. 2.8 we observe the minimum of the transition energy for $|0\rangle - |1\rangle$ transition at a half frustration point, usually called the qubit gap and labeled Δ.

Away from the symmetry point at $\Phi_0 = 1/2$ the additional energy term $\hbar\epsilon$ is added to the minimal energy splitting $\hbar\Delta$. It appears due to the coupling of the persistent current in the superconducting loop to the external magnetic field and can be calculated from

$$\hbar\epsilon = 2I_p(\Phi - \Phi_0), \tag{2.18}$$

where Φ is the external flux bias, I_p is the actual value of the current in the qubit loop, $\mathrm{I}_p = \mathrm{I}_c\sqrt{1 - \frac{1}{4\alpha^2}}$, and $\hbar\epsilon$ is usually called asymmetry energy.

The coupling strength of the persistent-current states and accordingly the qubit gap depend strongly on α. If α is smaller than 0.5 the barrier vanishes completely, as depicted in Fig. 2.9. If α=1 the barrier of the double-well potential profile becomes equal to the inter-cellar one. Therefore we should keep away from these limits, that is why in this work α-factors were chosen in the range between 67% and 71%.

The calculation shows dramatical influence of the α-factor on the energy splitting. It should be mentioned, that in our technical process $\alpha = 1\%$ is equal to 5 nm of the junction length. This means we should have carried out our lithography and evaporation process with 1 nm resolution.

In reality it is very difficult to achieve such a good resolution due to different factors, such as the secondary emission of

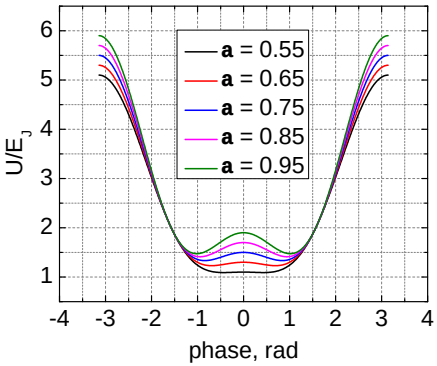

Figure 2.9: Energy profile of the flux qubit double-well potential shows the dependence of tunnel barrier from α.

electrons in resist materials during the lithography process, the difficulty in precise orientation of the chip in a sample holder of the evaporation setup, lift off crumbling edges of aluminum structures, etc. That is why after preliminary simulations, fabrication and measurements of flux qubits, the final fitting of spectroscopy curves were done in order to determine the real Josephson junction parameters.

2.3.3 Driven qubit

In order to understand the time evaluation of the system the simplified form of the Hamiltonian (2.17) is derived. For superconducting quantum circuits the flux qubit parameters are chosen in such a way, that the transition energy between the ground and excited state at the symmetry point $\Phi_0/2$ is at least several times smaller than that between $|1\rangle$ and $|2\rangle$ excited

state. Due to this fact, we can truncate the Hamiltonian taking into account only 2 lowest states and construct it using the qubit gap Δ and asymmetry energy ϵ:

$$H_t = \frac{\hbar}{2}\Delta\tilde{\sigma}_x + \frac{\hbar}{2}\epsilon\tilde{\sigma}_z, \tag{2.19}$$

here we used the labeling $\tilde{\sigma}_x = \left(\begin{smallmatrix} 0 & 1 \\ -1 & 0 \end{smallmatrix}\right)$ and $\tilde{\sigma}_z = \left(\begin{smallmatrix} 1 & 0 \\ 0 & 1 \end{smallmatrix}\right)$ for Pauli matrices.

If we want to diagonalize the Hamiltonian, we should use the unitary rotation R operator around the y axes by the angle $\theta = \frac{1}{2}\arctan(\Delta/\epsilon)$

$$R = \begin{pmatrix} \cos\theta & \sin\theta \\ -\sin\theta & \cos\theta \end{pmatrix}$$

By the rotation of the basis we go from the persistent-current states to the qubit states. The Hamiltonian will be represented in this case as

$$H_t = \frac{\hbar}{2}\sqrt{\Delta^2 + \epsilon^2} \tag{2.20}$$

and the qubit states appear in the persistent-current state basis as

$$|\uparrow\rangle = \cos\theta|l\rangle + \sin\theta|r\rangle \tag{2.21}$$

$$|\downarrow\rangle = -\sin\theta|l\rangle + \cos\theta|r\rangle \tag{2.22}$$

Here we can see that when $\theta = \pm\pi/4$, and, respectively, $\epsilon = 0$ we approach the symmetry point, and both qubit states turn into 0 because of the equal probabilities of $|\mathrm{l}\rangle$ and $|\mathrm{r}\rangle$. When ϵ is

large, $\theta \to 0$ and the qubit states tend to the persistent-current states.

If we now want to introduce the external drive to the system, we can perform it as a microwave signal, which will inductively couple to the qubit. This kind of excitation is important for spectroscopy and time-domain measurements. The Hamiltonian of a microwave signal can be written as

$$H_{mw} = \frac{A}{2}\cos(w_{mw}t + \phi)\tilde{\sigma_z} \tag{2.23}$$

where A, ω_{mw} and ϕ are the amplitude, the cycle frequency and the phase of the microwave signal. In the basis of the flux qubit states it will be represented as (after applying the rotation operator R):

$$\widehat{H_{mw}} = R^{\dagger}H_{mw}R = \frac{A}{2}\cos(w_{mw}t + \phi)\left[\frac{\epsilon}{w_q}\tilde{\sigma_x} + \frac{\epsilon}{w_q}\tilde{\sigma_z}\right] \tag{2.24}$$

where w_q is called the qubit frequency and is defined as

$$\omega_q = \sqrt{\Delta^2 + \epsilon^2}. \tag{2.25}$$

We can derive the solution for the driven system if we consider the influence of both Hamiltonians on it. The task is solved in [30] for the general case of driven two-level systems under several suppositions, called the rotate-wave approximation, and give the result in the form of

$$U(t) = \exp(-i\overrightarrow{\Omega}t\cdot\sigma/2), \tag{2.26}$$

$$\overrightarrow{\Omega} = (\frac{A\Delta}{2\hbar^2 w_q}\cos\phi, \frac{A\Delta}{2\hbar^2 w_q}\sin\phi, w_q - w_{mw}), \tag{2.27}$$

where $\overrightarrow{\Omega}$ defines the rotation axis, and $\overrightarrow{\sigma}$=(σ_x,σ_y,σ_z) is the vector of Pauli-matrices. If we want to drive the qubit in the sweet spot, meaning $\omega_{mw} = \omega_q$, the frequency of the oscillation will be

$$\Omega = \frac{A\Delta}{2\hbar^2 w_q}, \tag{2.28}$$

which is known as the Rabi frequency. Depending on the initial phase the rotation occurs around the x or y axis. In the general case far from the symmetry point the expression becomes more complicated:

$$\Omega = \sqrt{\left(\frac{A\Delta}{2\hbar^2 w_q}\right)^2 + (w_q - w_{mw})^2} \tag{2.29}$$

and is called the generalized Rabi frequency.

Under the influence of the constant resonant microwave signal the qubit is driven repeatable from the ground state $|0\rangle$ to the excited state $|1\rangle$. The average of these two states corresponds to $(|0\rangle + |1\rangle)/\sqrt{2}$ and obviously represents the current which differs from the ground state current of the qubit. This fact gives the opportunity to readout the qubit in the experiment.

2.4 π-junctions

In order to understand the origin of the π-junction phase shift in the flux qubit loop we will consider the microscopic description of 3d magnets. These kinds of magnets are metals such as Co, Ni, Fe and alloys such as CuNi. In our samples CuNi alloy was used as the material for π-junctions.

2.4.1 Itinerary 3d magnets

Metals, such as Co, Fe and Ni have a certain long-range ferromagnetic order of the momenta of collective electrons under a certain temperature, named Curie temperature. As the temperature increases, the thermal motion (or the entropy in other words), competes with the tendency of ferromagnetic dipoles to align and at higher temperatures the magnetic order will be destroyed. We will consider here the situation when the temperature is lower than Curie temperature.

The origin of the magnetism of 3d magnet alloys is based on the exchange interaction between the electrons of the 3d band. The exchange energy can be explained as the mere energy which is needed when the electron spins tend to gain the same orientation. Such configuration can be favorable because the magnetic ordering of the band electrons increases the kinetic energy of the system, but decreases its potential energy.

If we now consider the superconductor/ferromagnetic border, a Cooper pair can penetrate through the interface to some finite distance into the ferromagnet as well as it does through the interface superconductor/normal metal. The electron which has a spin aligned parallel to the exchange field will decrease its energy due to the exchange interaction. At the same time its kinetic energy will be increased. Also the electron with the spin aligned anti-parallel to the exchange field will compensate the amount of energy gained by the exchange interaction by decreasing its value of kinetic energy and momentum. As a result the whole Cooper pair will be shifted in the k-space, what will introduce an additional factor of $\exp^{i2q/h}$, where q is the acquired momentum of the pair and h is the Planck constant [31].

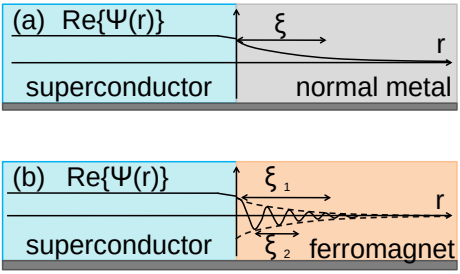

Figure 2.10: The behavior of the order parameter in the superconductor/normal metal and superconductor/ferromagnet stacks.

Finally, the order parameter in the ferromagnetic layer can be expressed as [32]

$$\Psi \sim \Delta \exp(-\frac{x}{\xi_1}) \cos(\frac{x}{\xi_2}) \tag{2.30}$$

and is depicted in Fig. 2.10.

2.4.2 Josephson energy of a π-junction

As it was already mentioned above, the Josephson equations (2.3) and (2.4) describe the behavior in the tunnel junctions consisting of superconductor-insulator-superconductor. In this case, I_c is positive and from (2.7) we can see that the Josephson energy possesses a minimum at $\psi = 0$. In the year 1977 it was shown by Bulaevski, Sobjanin and Buzdin that the supercurrent through the tunnel barrier with magnetic impurities can acquire a negative sign [33]. In this case the minimum of Josephson

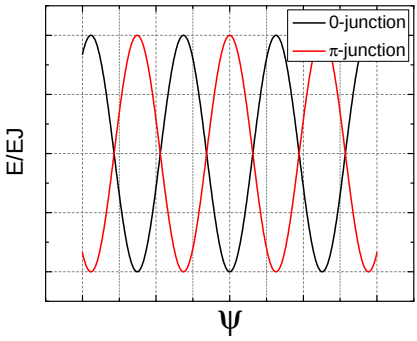

Figure 2.11: The graph of the energy of 0-Josephson junction and π-Josephson junction.

energy will occur at $\psi = \pi$ and actually is the ground state of the system, as shown in Fig. 2.11. This type of Josephson junctions got the name π-junctions, whereas the standard SIS junction got the name of 0-Josephson junction.

2.4.3 Proximity effect

If we will deposit a layer of a normal metal on the top of the superconducting material, the order parameter Ψ (2.1) will partly penetrate in the normal metal. This was already mentioned while describing the Josephson effect in Sec. 2.1.1. The characteristic length of the change of the order parameter is called ξ or the coherence length. If we then deposit another layer of the superconducting material over the normal metal/superconductor stack, and the thickness of the normal layer will be thin enough, two order parameters of both superconducting borders can

overlap. In this case the supercurrent can flow (Josephson effect).

In case of a ferromagnetic layer deposited on the superconductor the order parameter not only penetrates the ferromagnetic metal on the distance ξ_1, but also starts to oscillate with the characteristic period ξ_2, see Fig. 2.10.

2.4.4 CuNi

In the layers of classic ferromagnetic metals the coherence length ξ_1 is about 1 nm and it is problematic to fabricate Josephson SFS contacts with such a thickness of the interlayer. The $Cu_{0.x}Ni_{1-0.x}$ alloy has a Curie temperature of about 30-150 K and possesses weak ferromagnetic properties thus the supercurrent through 20 nm thick ferromagnetic layers can be observed. In our flux qubits the π-shift was created by 15 nm of the $Cu_{0.47}Ni_{0.53}$ alloy, placed between two Nb electrodes [34]. This alloy was thoroughly investigated and has clearly defined dependence of coherence length vs ferromagnetic layer thickness [16, 34].

2.4.5 Energy potential of the flux qubit with the π-junction

The π-junction, as the normal Josephson junction, can be modeled by the RSJ model [35], see Sec. 2.1.3 and Fig. 2.12

We still suppose that for our flux qubit the geometrical inductance is small. In case of the flux qubit loop interrupted by three SIS and one SFS Josephson junction the condition (2.15) will be reformed as

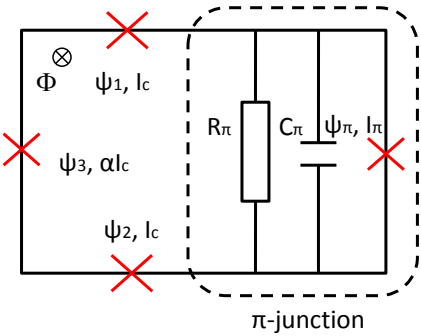

Figure 2.12: Flux qubit scheme with the π-junction. The shunt resistance represents the damping effects.

$$\psi_1 + \psi_2 + \psi_3 + \psi_\pi + 2\pi f = 2\pi N, \tag{2.31}$$

where $\psi_\pi = \pi$. As the phase of the π-junction is set constant by the fabrication process, the derivative of it is equal to zero and the kinetic energy (2.14) of the system doesn't change. But the potential energy U acquires an additional constant energy term $E_{J\pi}$, which shifts it in z-direction, thus causing the phase shift. The resulting energy profile, after the compilation of (2.6) and (2.31) will be described by:

$$U = E_J(2 + \alpha - 2\cos(\frac{\psi_1 + \psi_2}{2})\cos(\frac{\psi_1 - \psi_2}{2}) - \\ -\alpha\cos(2\pi f + \psi_\pi + 2\frac{\psi_1 + \psi_2}{2})) + 2E_{J\pi}, \tag{2.32}$$

where $E_{J\pi}$ is the Josephson energy of the π-junction. In this case, we will get the necessary working point in our double well

energy profile if the frustration $2\pi f + \psi_\pi$ will be 0, explaining the phase shift occurred because of the π-junction in the flux qubit.

2.5 Dispersive readout of flux qubits

2.5.1 Resonators

The next component of our design includes coplanar microwave $\lambda/4$-resonators used for the readout of our qubits.

Essentially, a microwave resonator can be represented with the equivalent electrical circuit from the appropriate resistance, inductance and capacitance, which can store energy. The advantage of the coplanar waveguide/resonator is that all of the conductors are situated on the same side of a dielectric substrate, and therefore can be fabricated in a single run. For the load circuit the resonator can act as a band pass filter, because it can block or pass a signal close to its resonant frequency.

One of the most important resonator characteristics is the quality factor Q:

$$Q = \omega \frac{\text{energy stored in the resonator}}{\text{rate of the energy loss from the resonator}}, \qquad (2.33)$$

where under the "rate of the energy loss from the resonator" one can understand the energy supplied by a generator per cycle to keep the amplitude of the transmitted signal constant.

The coplanar microwave resonator can be lossy due to the internal dissipation (crumbly edges, bad interface between the

metal and the substrate) and to the external load. The relationship between the "internal" ("unloaded") Q_{int}, "external" Q_{ext} and "loaded" Q_{load} quality factors can be written as

$$\frac{1}{Q_{load}} = \frac{1}{Q_{ext}} + \frac{1}{Q_{int}} \tag{2.34}$$

For us it is important to mention, that photons have the longer life time the higher the quality factor of a resonator is. Close to its resonance frequency the electrical response of any resonator can be modeled as a parallel combination of the capacitance C_r and inductance L_r. Its frequency can therefore be presented as

$$\omega_r = 2\pi\nu_r = \frac{1}{\sqrt{L_r C_r}}, \tag{2.35}$$

here we neglect the losses.

Quantum mechanically such a resonant circuit behaves as a harmonic oscillator and each single mode can be described by the Hamiltonian

$$H_r = \hbar\omega(a^\dagger a + \frac{1}{2}), \tag{2.36}$$

where a and $a^\dagger$ are the annihilation and creation operators.

2.5.2 Interaction of flux qubits with resonators

The interaction of a resonator and a flux qubit can be provided by the coupling of the magnetic fields generated by the qubit and the resonator. The resonator being coupled to the qubit, introduces the driving signal proportional to σ_z in the basis of the persistent-current states. The mechanism of the interaction

can be understood using Sec. 2.3.3 with the clarification that the field of the resonator represents a quantized field, being the array of modes and not the classical field.

The magnetic field of the critical current, which circulates in the qubit loop, couples to the magnetic field, appearing in the shorted resonator end after applying the microwave signal to the feed line. One can consider it as a magnetic dipole interaction μ_q and B_z of those and write an additional potential term as

$$U_m = -\mu_q B_z = I_p A_q B_r, \tag{2.37}$$

where I_p is the persistent current of the qubit and A_q is the area of the qubit loop. If we will introduce the mutual inductance $M_{r,q} = B_r A_q / I_r$, where I_r is the current in the shorted resonator end, we will rewrite the formula (2.37):

$$U_m = M_{r,q} I_p I_r. \tag{2.38}$$

The product of constants

$$\hbar\tilde{g} = M_{r,q} I_p I_0 \tag{2.39}$$

is called the bare coupling energy. $\mathrm{M}_{r,q}$ has here a meaning of the magnetic flux which enters the qubit loop per unit current in the shorted resonator end. I_0 represents zero-point or vacuum current fluctuations and can be calculated from $I_0^2/2L = \hbar\omega$, with ω being the angular frequency of the corresponding resonator mode. The actual transversal coupling will be

$$\hbar g = \hbar\tilde{g}\sin(2\theta), \tag{2.40}$$

with $\theta = \frac{1}{2}\arctan(\Delta/\epsilon)$ and depends on the asymmetry energy ϵ, thus being different for different magnetic flux qubit external bias.

2.5.3 Quantum mechanical description of the system resonator - flux qubit

The complete Hamiltonian of the system resonator - flux qubit will look like as following:

$$H_{q-r} = H_t + H_r + H_{int}, \tag{2.41}$$

where H_t and H_r are defined in (2.19) and (2.36), respectively. The term which describes the interaction of the resonator and Hamiltonian is shown in [36]:

$$H_{int} = -\hbar g(a^\dagger + a)\sigma_z, \tag{2.42}$$

and can be interpreted as a coherent exchange of the excitations between the resonator and the flux qubit.

In the case of dissipation, the Hamiltonian (2.41) will include also terms, which will characterize the relaxation and the dephasing of both the resonator and the qubit due to the environment. In the absence of damping, see [36, 37], it is possible after the exact diagonalization of the Hamiltonian (2.41) to obtain the excited eigenstates, so-called dressed states of the system:

$$|+, n\rangle = \cos\vartheta_n|g, n\rangle + \sin\vartheta_n|e, n+1\rangle, \tag{2.43}$$

$$|-, n\rangle = -\sin\vartheta_n|g, n\rangle + \cos\vartheta_n|e, n+1\rangle; \tag{2.44}$$

and the ground state $|e,0\rangle$, with the angle

$$\vartheta_n = \frac{1}{2}\arctan\left(\frac{2g\sqrt{n+1}}{\omega_{rq}}\right) \tag{2.45}$$

and corresponding eigenenergies

$$E_{\pm,n} = (n+1)\hbar\omega_r \pm \frac{\hbar}{2}\sqrt{4g^2(n+1)+\omega_{rq}}, \tag{2.46}$$

$$E_{e,0} = -\frac{\hbar\omega_{rq}}{2}, \tag{2.47}$$

where n is the resonator energy state in the harmonic oscillator energy ladder, n = 0...∞, e and g are the excited and ground state of the flux qubit, respectively. $|g,n\rangle$=$|g\rangle\otimes|n\rangle$ and $|e,n\rangle$=$|e\rangle\otimes|n\rangle$ label the basis states of the bare qubit and the resonator system. The strength of the flux qubit-resonator coupling g was introduced in (2.39) and (2.40), $\omega_{rq} = \omega_r - \omega_q$ is the detuning parameter, showing how far is the resonator detuned from the flux qubit gap Δ.

Two limits of detuning for the qubit-resonator system are depicted in Figs. 2.13, 2.14. In the first case $\omega_r = \omega_q$ and the degeneracy between the energies of the two dressed states (2.47) will be lifted by the factor $2g\sqrt{n+1}$ because of the flux qubit - resonator interaction.

In the case of a single excitation, from (2.47) we will obtain the expressions for the eigenstates

$$|\pm,0\rangle = \frac{1}{\sqrt{2}}(|g,1\rangle + |e,0\rangle), \tag{2.48}$$

what can be interpreted as flopping the initial state of the excited qubit and zero photons in resonators |e,0⟩ to the 1-photon state in the resonator |g,1⟩ and back.

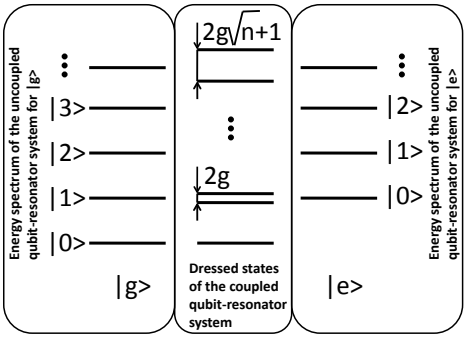

Figure 2.13: Energy spectrum for uncoupled and coupled resonator-flux qubit states for zero detuning $\omega_r = \omega_q$.

For the case, when the detuning is much larger one can expand formula (2.47) in the Taylor's series around the point $4g^2(n+1)/\omega_{rq}^2 \to 0$. Further $\mathrm{E}_{\pm,n}$ will be presented as

$$E_{\pm,n} = \hbar\omega_r(n+1) \pm \frac{\hbar\omega_{rq}}{2} \pm \frac{\hbar g^2(n+1)}{\omega_{rq}} \mp ... \qquad (2.49)$$

From this expression we can clearly see, that:

1) The energy gap of the flux qubit gets a shift, proportional to g^2/ω_{rq}. It is called Zeeman or Stark shift depending on its nature - magnetic or electric, respectively. The detailed formula, derived from (2.49) truncated to the first Taylor's order will appear to be

$$E_{+,n} - E_{-,n-1} = \hbar\omega_q + \frac{g^2\hbar(2n-1)}{\omega_{rq}} + ... \qquad (2.50)$$

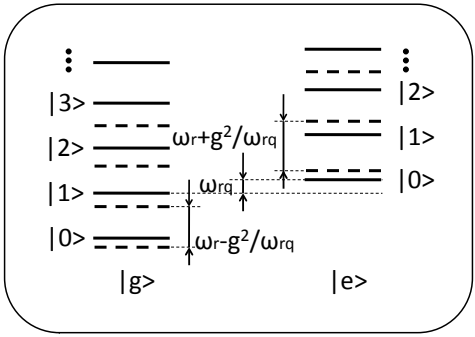

Figure 2.14: Energy spectrum of the dressed states of the system resonator-flux qubit (dashed lines) in the dispersive regime, when $g^2/\omega_{rq} \ll 1$.

and depends on the state of the resonator.

2) The neighbor energy levels of the resonator for the definite flux qubit energy states are also shifted. Using (2.49) one more time we will obtain

$$E_{+,n} - E_{+,n-1} = \hbar\omega_r + \frac{g^2\hbar}{\omega_{rq}} + ... \tag{2.51}$$

$$E_{-,n} - E_{-,n-1} = \hbar\omega_r - \frac{g^2\hbar}{\omega_{rq}} + ... \tag{2.52}$$

We can see that the shift depends on the state of the qubit and the detuning.

In case of the truncation to two levels, using the Taylor's series for (2.45) and (2.47) we will get the new expression for the dressed states:

$$|-,0\rangle = \frac{-g}{\Delta}|g,0\rangle + |e,1\rangle, \tag{2.53}$$

$$|+,0\rangle = |g,1\rangle + \frac{g}{\Delta}|e,0\rangle. \tag{2.54}$$

The situation is represented in details in Fig. 2.14.

2.5.4 Dispersive shift measurements

The flux qubit state dependence on the resonator, described by (2.52) can be used for detecting the flux qubit state. We can send the microwave signal through the transmission line and measure the reflected or transmitted signal.

In our case, the amplitude A and phase ϕ of the microwave signal transmitted through the feed line is measured versus the probe signal. In our setup the flux qubit acts as an effective inductance, which depends on its eigenstates σ_z, coupling strength g and detuning ω_{rq}. This variable inductance changes the resonator frequency and its transmission spectrum according to the model (2.35). For the far-detuned limit $g^2/\omega_{rq} \ll 1$ the amplitude shifts of the resonator frequency are illustrated in Fig. 2.15.

The width of the resonant peak is defined by the loss rate: $\kappa_{loss} = \omega_r/\mathrm{Q}_{load}$. If $\kappa_{loss} < g^2/\omega_{rq}$, the dips which represent the ground and excited state of the qubit are resolvable. In the limit of $\kappa_{loss} > g^2/\omega_{rq}$, the dips overlap and the amplitude contrast decreases.

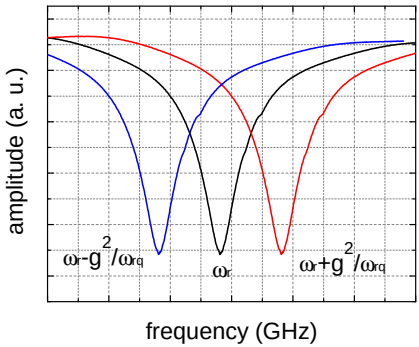

Figure 2.15: Illustration of a dispersive shift of the resonator frequency, attributed to two qubit states. If the shift is smaller than the broadening of the resonator dip, the signal becomes hardly resolvable.

2.6 Decoherence of the flux qubit

2.6.1 Bloch sphere

An arbitrary single state of the flux qubit can be represented by a vector $|\Psi\rangle$ in a Hilbert space. Spanned in the flux qubit basis of eigenstates - ground $|g\rangle$ and excited $|e\rangle$ states, the vector of qubit state will look like

$$|\Psi\rangle = a|g\rangle + b|e\rangle, \tag{2.55}$$

where a and b can be complex, and the square of coefficients a^2 and b^2 have the meaning of a probability to find a qubit state in the state $|g\rangle$ or $|e\rangle$, respectively. Logically, these probabilities being summed give one, $a^2 + b^2 = 1$. In the measurements it is possible to obtain only the absolute value of weights, that

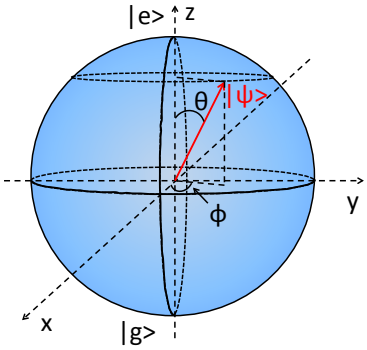

Figure 2.16: The representation of the qubit state with a Bloch sphere. The ground state is a vector, pointing to the south pole, and the excited state is a vector, pointing to the north pole.

is why it is the difference in phase between coefficients what matters. With these two conditions originally four dimensional space can be reduced to two dimensions.

For the efficient understanding of the flux qubit dynamics and decoherence processes it is useful to imagine the quantum state of the qubit as a Bloch sphere. If the qubit exists in the pure state, the end point of the vector $|\Psi\rangle$ is situated on the surface of the unit sphere (see Fig. 2.16). In case of the dressed state, decoherence processes or other interactions with the environment, the end of the Bloch vector can be situated in any point inside the Bloch sphere.

As it is illustrated in Fig. 2.16, in terms of angles ϕ and Θ the qubit state can be represented as

$$|\Psi\rangle = \cos\frac{\Theta}{2}|g\rangle + e^{i\phi}\sin\frac{\Theta}{2}|e\rangle, \tag{2.56}$$

with the angle Θ defined as $\Theta = \frac{1}{2}\arctan(\Delta/\epsilon)$ for the flux qubit.

If we will square the vector $|\Psi\rangle$ and project it on the z-axis, we will get the occupation probability of the two logic states of the flux qubit, $p_g = \cos^2\frac{\Theta}{2}$ and $p_e = \sin^2\frac{\Theta}{2}$.

2.6.2 Larmour precession of the flux qubit

As it was mentioned before, with the help of the Bloch sphere and two angles ϕ and Θ one can describe the pure qubit state. It turns out, that ϕ (representing the phase difference between the two states of the superposition) evolves with time, causing the precession of the qubit with the constant frequency. Let us suppose that the Hamiltonian of the system answers the stationary Schroedinger equation $\widehat{H}|\Psi(t)\rangle = E\Psi(t)$. The Schroedinger equation which describes the evolution of the system in time [38] looks like:

$$\widehat{H}|\Psi(t)\rangle = i\hbar\frac{\partial}{\partial t}|\Psi(t)\rangle \tag{2.57}$$

If we know the flux qubit state at the time moment $t = 0$, like it is described in (2.56), we will be able to integrate (2.57) and apply to this flux qubit state the operator:

$$\begin{aligned} e^{i\widehat{H}t/\hbar}|\Psi(t)\rangle &= e^{i\widehat{H}t/\hbar}(\cos\frac{\Theta}{2}|g\rangle + e^{i\phi}\sin\frac{\Theta}{2}|e\rangle) = \\ &= e^{iE_gt/\hbar}\cos\frac{\Theta}{2}|g\rangle + e^{iE_et/\hbar}e^{i\phi}\sin\frac{\Theta}{2}|e\rangle) = \\ &= e^{iE_gt/\hbar}(\cos\frac{\Theta}{2}|g\rangle + e^{-i(\Delta+\phi)/t}\sin\frac{\Theta}{2}|e\rangle), \end{aligned} \tag{2.58}$$

where $\hbar\Delta = E_e - E_g$ is the energy gap of the qubit. We see from the equation, that the phase difference evolves with the frequency

$$\omega_L = \Delta, \tag{2.59}$$

called the Larmour frequency.

Further, for the ease of understanding, we will always consider ourselves in the frame, which precesses with the Larmour frequency, therefore watching the Bloch vector disregarding this constant precession.

2.6.3 Rabi frequency

From the previous section it is clear, that for measurements of the qubit $|\mathrm{g}\rangle \rightarrow |\mathrm{e}\rangle$ transitions one should first apply a resonant oscillating field which will match the Larmour frequency. By doing this we will set us in the rotating frame of the flux qubit, described by the Bloch sphere.

Further, for inducing the transition from the ground to the excited state of the flux qubit, the microwave signal in the flux-direction (z-axis in Fig. 2.16) should be applied [39]:

$$\delta\Phi_{mw} = |\Phi_{mw}| sin(\omega_{mw} t + \phi_{mw}), \tag{2.60}$$

where ϕ_{mw} determines the rotation axis in the xy-plane of the qubit.

The modulation of the magnetic field through the qubit loop

$$\delta\epsilon_{mw} = 2I_p \delta\Phi_{mw}, \tag{2.61}$$

where I_p is the persistent current in the qubit loop. Exactly at the resonance when $\omega_{mw} = \omega_L$ and in the degeneracy point the

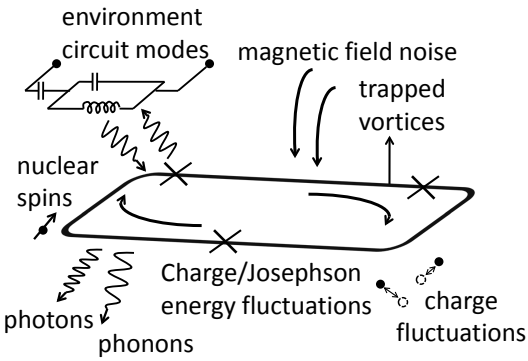

Figure 2.17: Potential noise sources influencing the flux qubit.

expression for the Rabi frequency - the frequency of flipping the flux qubit from the ground to the excited state - will be represented by

$$\Omega_{R,\epsilon} = \frac{I_p|\Phi_{mw}|}{\hbar}\frac{\Delta}{\sqrt{\epsilon^2+\Delta^2}}. \tag{2.62}$$

what shows, that far from the degeneracy point the Rabi frequency drops with Δ/ϵ.

2.6.4 Possible noise sources

As discussed above, two different states $|g\rangle$ and $|e\rangle$ of the flux qubit have different energies. The dispersive measurement technique uses microwave signals in order to realize the transition between the states, but in principle, there exists a lot of noise in the environment, which can affect the qubit states [40]. Possible sources of noise are shown in Fig. 2.17.

It is used to distinguish two main categories of the noise sources, by the possibility to influence on their presence in the circuit.

First type of the noise is called circuit noise and has been investigated for a long time being reviewed in details in [41]. It includes all kinds of noise, which originate from the necessities to control and readout the qubit state. One can design stronger or weaker coupling of the flux qubit therefore also influencing the outer circuit noise effects on the quantum circuit. Amplifiers or signal generators give a combination of white and 1/F noise, one should also take into account the ohmic noise with its white power spectrum.

The second group - so called non-circuit-noise - can be subdivided to microscopic and macroscopic sources. The main difficulty here is the low possibility to control its coupling to the qubit. Microscopic noise can be caused by charge fluctuations, trapped vortices, nuclear spins or defects in tunnel barriers. Choosing the right material can help to eliminate this kind of sources, but for some technological processes it is not possible to change the materials. Microscopically 1/F noise can disturb the system, and its origin is not quite well understood.

Different sources of noise can influence the flux qubit differently, causing the shift of the azimuthal angle ϕ or longitudinal angle Θ, corresponding to quantum dephasing and the energy relaxation consequently, see Fig. 2.18.

This can lead, for example, to the shift of the Bloch vector from the initial rotating frame, spoiling manipulations with the qubit.

All the noise influences, mentioned above, are referred to the decoherence of the flux qubit and lead to the loss of the quantum information, stored in it. There are also other factors

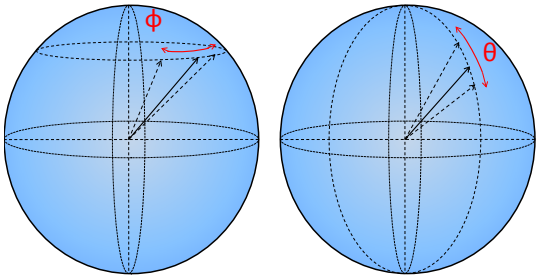

Figure 2.18: a) Fluctuation in biasing of flux qubit leads to the modulation of the Larmour frequency, which in turn, causes the uncertainty in the qubit phase ϕ. b) Due to the exchange of the energy with the environment the flux qubit can absorb or emit a photon (this complex process is called depolarization). As a result, the qubit parameter Θ is disturbed.

appearing to be sources of errors - errors of preparing the qubit in the initial state, measurement inaccuracies and errors in the excitation of microwave signals. As one can see, there is a large number of sources, which can spoil the ideal dynamic of the flux qubit and limit the number of possible operations.

2.6.5 Description of decoherence

For the description of the decoherence of the flux qubit one needs to take into account both the longitudinal relaxation (depolarisation), $\Gamma_1 = T_1^{-1}$ and the transverse relaxation (dephasing), $\Gamma_2 = T_2^{-1}$. So-called pure dephasing Γ_ϕ can also happen, for example, under the condition of longitudinal low-

frequency noise. Variables with the index "$\perp$" will be further referred as variables, corresponded to the depolarization and those with the "||" index will be attributed to the pure dephasing, respectively. The resulting rate of the general dephasing process will be described by

$$\Gamma_2 = T_2^{-1} = \Gamma_\phi + \frac{1}{2}\Gamma_1. \tag{2.63}$$

The detailed theoretical description of the decoherence is given in [42]. The theory implies several conditions: the disturbing noise is weak, it is short-correlated and its spectral density has a smooth profile for all frequencies from zero to frequencies of the order of Γ_ϕ. It was written that each noise source can be conveniently described by its quantum spectral density $S_\lambda(\omega)$:

$$S_\lambda(\omega) = \frac{1}{2\pi}\int \langle \widehat{\delta\lambda}(0)\widehat{\delta\lambda}(t)\rangle e^{-i\omega t}dt, \tag{2.64}$$

where λ is the normalized external parameter, which describes the influence of the noise on the properties of the flux qubit, for example, flux noise f_ϵ. In general, λ can present any fluctuation, and it doesn't matter if it has circuit, microscopic or macroscopic nature. $\widehat{\delta\lambda}$ is the operator acting on the environmental variables.

Using these terms, the relaxation and dephasing times can be rewritten as

$$\Gamma_1(\nu) = \frac{\pi}{2}D^2_{\lambda,\perp}S_\lambda(\nu), \tag{2.65}$$

$$\Gamma_\phi(\nu) = \pi D^2_{\lambda,||}S_\lambda(0), \tag{2.66}$$

where ν is the qubit frequency and as the relaxation is only sensitive to the noise at the qubit frequency, the noise frequency

as well. The factors $D_{\lambda,\perp}$ and $D_{\lambda,||}$ take into account the qubit sensitivity in the transverse and longitudinal directions. They are expressed as

$$D_{\lambda,\perp} = \frac{1}{h}(\frac{\partial H}{\partial \lambda})_{\perp} = \frac{1}{h}|\langle \Psi_g|\frac{\partial H}{\partial \lambda}|\Psi_e\rangle|, \quad (2.67)$$

$$D_{\lambda,||} = \frac{1}{h}(\frac{\partial H}{\partial \lambda})_{||} = \frac{1}{h}|\langle \Psi_g|\frac{\partial H}{\partial \lambda}|\Psi_g\rangle - \langle \Psi_e|\frac{\partial H}{\partial \lambda}|\Psi_e\rangle|. \quad (2.68)$$

2.6.6 Decoherence in the flux qubits with the π-junctions

As it was mentioned in Sec. 1, flux qubits with π-junctions were proposed to eliminate the flux noise from the flux qubit environment. In [35] was suggested that the difficulty can appear from the noise, created by the π-junction itself.

The expression for the effective noise spectrum, which was obtained by Kato, Golubov and Nakamura, looked like:

$$J_{eff}(\omega) = \frac{8E_J^2 E_{C,\pi}}{\hbar^3}\frac{\gamma\omega}{\gamma^2\omega^2 + (\omega^2 - \omega_0^2)}, \quad (2.69)$$

where E_j is the Josephson energy of the big aluminum Josephson junction in the flux qubit loop, $E_{C,\pi} = \frac{e^2}{2C_\pi}$, C_π is the π-junction capacitance, $\gamma = \frac{1}{R_{N,\pi}C_\pi}$, $R_{N,\pi}$ is the normal state resistance of the π-junction, $\omega_0 = \frac{\sqrt{8E_{J,\pi}E_{C,\pi}}}{\hbar}$, and $E_{J,\pi}$ is the Josephson energy of the π-junction.

The relaxation time is given by

$$\Gamma_1 = T_1^{-1} = 2J_{eff}(\Delta/\hbar)\coth(\frac{\Delta}{2k_BT}), \quad (2.70)$$

where by Δ is labeled the qubit energy gap.

The formula was derived under an assumption that $E_C \ll E_J \ll E_{J,\pi}$, what means, that the π-junction operates in the stable-phase regime.

In our experiments C_π is very small, of the order of about 30 fF, and assuming that $\omega \ll \omega_0$, $E_J = \frac{I_c \Phi_0}{2\pi} = \frac{I_c \hbar}{2e}$ and $\omega = \frac{\Delta}{\hbar} 2$ we can make an estimation of the relaxation times for our particular designs. For our π- and 0-junctions we usually had $I_\pi \approx 6.2\,\mathrm{mA}, E_{J,\pi} \approx 2{\cdot}10^{-18}\,\mathrm{J}, E_{C,\pi} \approx 3{\cdot}10^{-25}\,\mathrm{J}, I_c \approx 1.25\,\mu\mathrm{A}$, consequently $E_J \approx 3{\cdot}10^{-22}$ J. We can see, that for our samples the assumption $E_C \ll E_J \ll E_{J,\pi}$ is true, and we could estimate the relaxation time $T_1 \approx 42$ ns.

2.7 Conclusion

In this chapter we discussed the classical Josephson junction model and quantum mechanical description of the flux qubit. We also considered the origin of the π-shift in SFS Josephson junctions and described the implementation of the π-junction in the flux qubit loop for creating the internal π phase shift to the symmetry point of the flux qubit. The basic ideas of the noise theory in the flux qubits and its approach for the flux qubits with the π-junctions were introduced. It was shown, that for longer coherence times of the latter one needs to have large Josephson energy and small normal-state resistance of the π-junction.

3 Fabrication of Flux Qubits

In this chapter, the fabrication process of flux qubits with π-junctions will be considered. In our case, the Nb-part of a qubit with a π-junction is needed to be connected with the aluminum part. The niobium part with $\lambda/4$-resonators and π-junctions was made in the group of Prof. Ryazanov in Chernogolovka, Russia. The fabrication process is described in (3.1). Further, samples were transfered to Karlsruhe. The aluminum part was fabricated in the Karlsruhe Institute of Technology and consisted of half a flux qubit loop interrupted by 3 Josephson junctions. For this aim, double-angle shadow evaporation in an MMA/PMMA resist stack with residual PMMA bridges was applied.

The main problem was to remove NbO_x, which naturally formed right after exposing the Nb layer to air. It should have been etched out in-situ right before the Al evaporation step. Using a high-energy constant Ar beam etching was not an option, because it could destroy the residual PMMA bridges, which are essential for the two-angle shadow evaporation. That is why in addition to the standard thin-film technique, a special in-situ low-energy Ar etching procedure of NbO_x was developed in order to make the contact between Al and Nb transparent. For this aim, the hard-mask technique is also suitable and will be discussed in the last subsections of this chapter.

The technique was first tested on Josephson junctions evaporated on Nb pads, forming hybrid Nb/Al/AlO_x/Al/Nb Josephson junctions. Their IV characteristics were measured using a four-point configuration in current-bias mode.

3.1 Nb layer fabrication

The fabrication technology of Nb $\lambda/4$ resonators (2.5.1) with π-junctions near their shorted ends included several substeps.

On the fist step, the Nb/CuNi/Nb trilayer was deposited. The process was held in an Ar atmosphere, and whereas Nb layers were fabricated by DC magnetron sputtering, $Cu_{0.47}Ni_{0.53}$ was deposited by rf-sputtering after cleaning of the niobium surface. The critical current of the Nb/CuNi/Nb junction was aimed to be 3.7 kA/cm^2 [43]. The thickness of the Nb layers was 150 nm, for $Cu_{0.47}Ni_{0.53}$ it was 15 nm. Further, mesas of π-junctions were formed with the help of optical lithography and plasma etching. The mesas had the form of squares with areas of 8×8, 10×10 and 14×14 μm^2. The lithography process with plasma etching was repeated in order to form the bottom resonator layer. After that, a 350 nm thick spacing layer of SiO_x was deposited and formed with the help of thermal sputtering, lithography and lift-off. SiO_x was used in order to isolate the bottom Nb layer from the upper wiring Nb layer. Finally, the upper niobium wiring of 450 nm thickness was fabricated using DC magnetron sputtering and optical lithography with following lift-off treatment. The samples were then spin-coated for surface protection and shipped to Germany for following fabrication steps.

3.2 Spin-coating

To form sub-micron aluminum structures with Josephson junctions, electron beam lithography should be used. The principle of creating patterns is to expose a polymer resist layer to an electron beam at a certain accelerating voltage, exposure time and step area. Due to weak bonds between monomers of polymer [44], resist materials are sensitive to e-beam exposure and temperature (see Fig. 3.1).

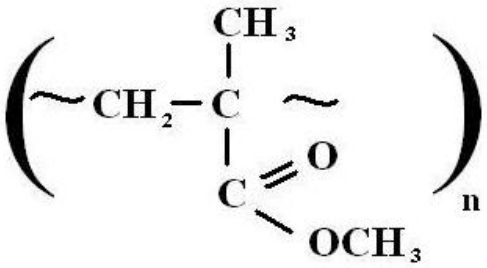

Figure 3.1: Chemical formula of PMMA. PMMA has weak bonds between monomers which break under electron beam exposure 3.1.

To obtain the residual bridge which was later used for shadow evaporation and formation of Josephson junctions, a two-layer resist stack was spin-coated. We used MMA (8.5) MMA EL11 positive resist (methylmetaacrylate-co-methylacrylate acid in 89 % ethyl lactate) for the first layer, spin-coated at 4000 rpm for 90 s. The corresponding thickness for these parameters was around 470 nm. For the second layer, PMMA 950K A4 (polymethylmethacrilat with molecular mass 950 g/mol solved in 98 % anisol) was used, and it was spin-coated with the same recipe to a thickness of approximately 220 nm. Both thicknesses

are important to know in order to estimate the angles in double-angle evaporation, which will be discussed later. Data sheets on both polymer and copolymer can be found in [45].

After spin-coating, the sample was baked in an oven in order to evaporate the residual solvent. For both anysol and ethyl lactate, the boiling temperature is about 155 °C, the time of the bake in recipes varied from 30 to 55 min. However, the baking conditions were changed due to the presence of the π-junctions on the chip. The CuNi thickness decreases at temperatures exceeding 100 °C due to the atom migration into the neighboring Nb layers, and consequently, the internal phase bias of the loop can be changed, transforming a π-junction into a 0-junction [16]. That is why the first set of samples was baked in the oven for just 30 min at 130 °C temperature. For the germanium mask technique this temperature is too low leaving a lot of solvent in the resist layers. The residual anysol in MMA evaporates under the germanium layer forming bubbles, that is why for a final set of samples 155 °C bake temperature was used.

3.3 Lithography step

After resist application, the chip is positioned in an SEM vacuum chamber. The lithography machine is a scanning electron microscope LEO 1530 [46] located at Institute of Nanotechnology (INT) and equipped with an additional electrically driven piezo nanostage. Structure positioning is performed with an accuracy of about several tenth of nm. For structure writing Elphy Plus software from Raith GmbH is used [47]. To expose the two-layer PMMA/MMA stack, an electron acceleration

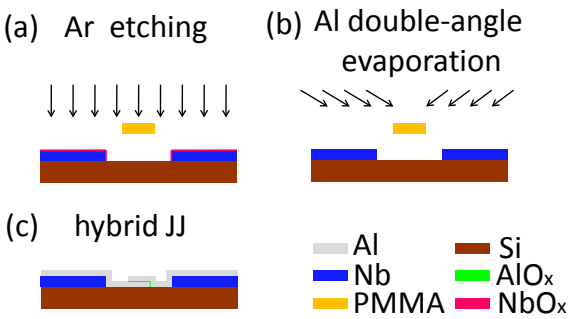

Figure 3.2: PMMA bridge over silicon substrate after development, Ar etching and Al two-angle shadow evaporation. The PMMA/MMA thickness ratio defines the angle of shadow evaporation. Parameters of the Ar cleaning: 1 kV of acceleration voltage in 4 periods of 30 seconds interrupted by pauses of 1 min at Ar pressure of about 8.6×10^{-5} mbar.

voltage of 30 kV was used. The necessary dose factor was determined with a standard dose test procedure, writing a series of thin structures with doses varying from 1.00×260 μCl/s·cm^2 till 1.35×260 μCl/s·cm^2 in steps of 0.05×260 μCl/s·cm^2.

The electron beam breaks some chemical bonds in PMMA, shortening the polymer chains. The beam by itself is about 3 nm in diameter, but the major effect is caused by secondary emitted electrons. Therefore, the minimal feature size to be written is about 60 nm at 30 kV accelerating voltage. The later dissolution of the exposed resist is much easier than of the

non-exposed one and is called development. We developed our structures in a mixture of isomethylbythilketon (MIBK) and isopropanol (IPA) with a volume ratio of 1:3 for 57 seconds. After that, the sample is placed in pure IPA for 2 minutes in order to stop the developing process. Finally, it is dried under N_2 flow.

The co-polymer MMA needs much less exposure energy for chemical bonds to be broken than PMMA. So after the development we get a pattern of our design written on PMMA in 1:1 scale and MMA gives wider openings under it. In particular, for the Josephson junction areas we get only 200 nm thick nanobridges, while 470 nm of MMA in this area were totally dissolved giving the space for the formation of Josephson junctions under the two oblique angles, see Fig. 3.2.

3.4 Evaporation step

After the development of the PMMA/MMA stack we obtained the design transferred to our silicon substrate. For evaporation of Al, we put the sample in a ultra high vacuum system, which is shown in Fig. 3.3. The main requirements necessary for our process are the availability of a load-lock and an ultra high vacuum evaporation chamber, liquid nitrogen cooling of the sample down to -150 °C, in-situ Ar etching with a directed Ar beam in the load lock, fine angle alignment for double-angle shadow evaporation and oxidation in the load lock with manual control of the O_2 pressure.

One of the most important characteristics of the evaporation set-up for fabrication of the high-quality tunnel junctions is the pressure in the high-vacuum chamber where the evaporation

of aluminum takes place. In the set-up which we used at INT, a vacuum of about $2{\cdot}10^{-10}$ mbar can be reached, although $2{\cdot}10^{-8}$ mbar is enough for obtaining high-quality Al Josephson junctions. Unfortunately, the maximum oxidation pressure which can be reached in the load-lock was $1.4{\cdot}10^{-2}$ mbar of pure O_2 flow,what together with used oxidation time defined the minimum value of our junction critical current.

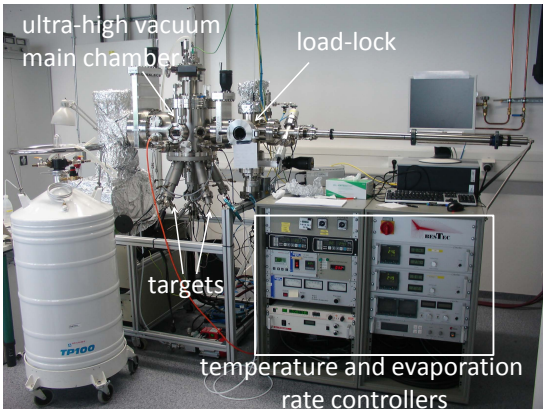

Figure 3.3: Evaporation set-up.

Now it is important to mention, that if one needs to place only an aluminum flux qubit at the right place near the resonator, one isn't necessarily obligated to pre-clean the surface of the sample with the directed Ar beam. In this case, the qubit spectroscopy line is expected to be wider because the coherence time of the qubit is shortened due to the imperfection of the interface between the silicon substrate and aluminum. It can be explained by the fact, that dielectric losses appear due to resonant absorption of the microwave radiation by two-level systems (TLS), possessing an electric dipole moment [48]. It

was shown in [49] and [50], that this can be a dominant loss mechanism and can be caused by TLS in the bulk dielectric substrate, at the metal-dielectric interface or in a thin layer on the metal and dielectric surfaces exposed to air. Flux qubits, as nonlinear microwave resonators, are suffering from the same problems [51, 52].

Fabrication process for Al-based flux qubits was established, and the spectroscopy plot of the flux qubit (see Fig. 3.6) was successfully measured, as illustrated in Fig. 5.10.

However, for the pre-fabricated trilayer design, where one part of the flux qubit is a Nb strip with the π-junction, one needs a cleaning step, as it was already mentioned in the introduction to this chapter.

After fixing the sample in the sample-holder and installing it into the load lock, the pressure is pumped down to 10^{-6} mbar. The surface of the sample was cleaned with a directed argon beam for 2 min at 1kV of acceleration voltage. As it was mentioned, the high Ar beam energy easily destroys the PMMA bridge. In order to find the optimum, several parameters were varied, and after a number of attempts the following procedure was developed.

On the first step, the sample is pre-cooled for 1 hour in the main chamber of the evaporation setup at high vacuum at a temperature of about -120 °C. This step is necessary to protect the sample from overheating during the following Ar beam etching procedure. Further, the sample is transported to the load lock, where it is etched in 4 periods of 30 seconds interrupted by pauses of 1 min in order to prevent the resist stack from melting. The Ar is flowing in the load lock and the pressure is held at the value of $6.3 - 8.6 \cdot 10^{-5}$ mbar, the distance between the Ar source and the chip is about 7 cm. The

accelerating voltage was 1 kV, yielding a current obtained by the sample-holder electrode of around $52 - 66$ mkA.

On the next step, the sample is transferred into the main chamber, which was always held under $10^{-9} - 10^{-10}$ mbar pressure. For the evaporation step the sample was pre-cooled one more time for 1 hour at a temperature of about -120 °C. At lower temperatures, the film roughness reduces significantly. The angle calculation for the evaporation step was performed with a non-commercial software which took into account the angle of the sample-holder, the spacious angle of the target and the thickness ratio of the resist stack. The angle of the sample can be adjusted with a micrometer screw.

The first layer of Al was evaporated under the oblique angle, forming an aluminum wire 1 μm wide and 30 nm thick with an interruption on the place of the Josephson junction. The Al layer is then oxidized in-situ, admitting the pressure of $1.4{\cdot}10^2$ mbar of pure oxygen for about 5 minutes. Subsequently, another 30 nm layer of aluminum are evaporated from the different angle, forming the tunnel contact with the area of about $0.2{\times}1$ μm^2 (see Fig. 3.4).

Sample parameters such as contact areas, resistivities, etc., varied slightly between fabrication batches.

On the first and second steps of Al evaporation, the angles were adjusted to $327° + 1'$ and $327° + 0.4' + 20''$, an Aluminum target temperature was $1170 - 1176$ °C, main chamber pressure was about $4{\cdot}10^{-9}$ mbar, and the rate varied between 6 and 8 nm/min. To warm the sample, it is held in the load-lock under nitrogen flow for 15 minutes. After that, the sample is taken out and put in acetone. Due to the Ar treatment, the resist stack became harder and more fragile, increasing the duration of the lift-off process from 10 min to almost 45 minutes. Then the

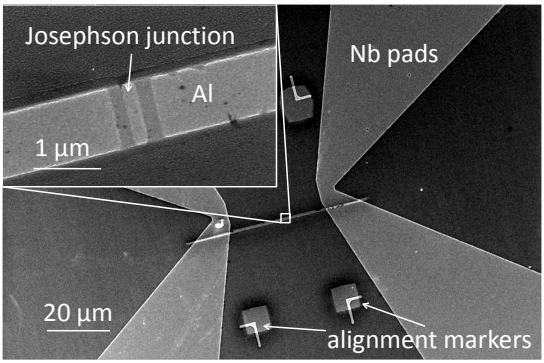

Figure 3.4: SEM picture of 1 μm wide Al strip on the Nb pads. The inset shows a Josephson junction.

sample was rinsed with isopropanol and dried under nitrogen flow.

To inspect the geometrical quality of the junction, the scanning electron microscope (SEM) "Leo" located at INT is used. The images were made at 10 kV accelerating voltage. The optical microscope picture and SEM micrograph of Josephson junctions of the hybrid flux qubits which later showed nice spectroscopy results are depicted in Fig. 3.5.

3.5 Germanium hard mask technique

The technique which was mentioned above gave us the possibility to measure the first flux qubit containing a π-junction, what is discussed in Sec. 5.4.

The process gave nice and reproducible results on hybrid test Nb/Al/AlO_x/Al/Nb junctions, as well as flux qubits with just

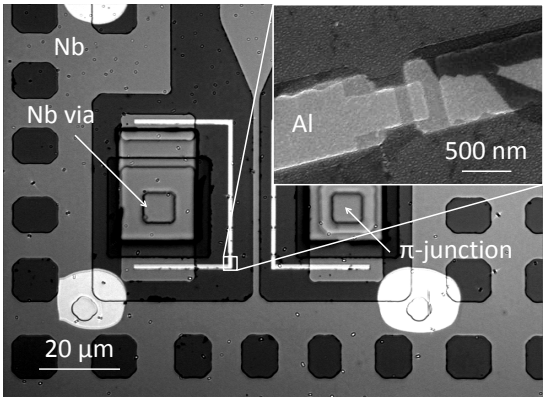

Figure 3.5: The flux qubit with π-junction (right) and without π-junction (left) are situated near the shorted end of the $\lambda/4$ resonator. The inset shows one of the large Josephson junctions of the flux qubit without π-junction.

the Nb strip without π-junctions. On the flux qubit with π-junction the residual PMMA bridges were sometimes destroyed, as shown in Fig. 3.7. Here one can clearly see some kind of short between the Al borders of the Josephson junction. Presumably, the problem had the following origin. In our experiments, the bottom layer of Nb had a thickness of about 150 nm. On the other hand, the stack of the π-junction with the spacing layer of SiO_x had about 1 μm height. This thickness can already give a significant tilt of the resist in an area of several tenth μm around the junction and can thus cause some stress in the residual PMMA bridge. Although the measurements showed that this short was oxidized and the tunnel barrier did exist, we had to modify the process in order to obtain Al Josephson junctions with precisely defined areas.

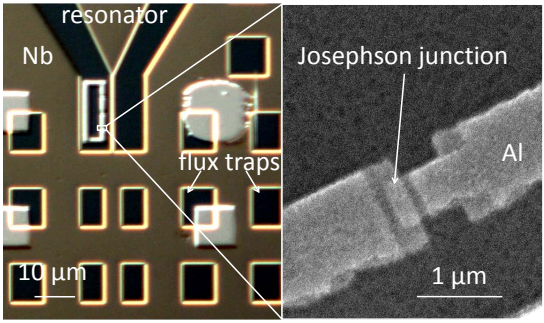

Figure 3.6: Photo of the flux qubit made completely from Aluminum in Nb dispersive readout scheme, sample #1, resonator #1.

3.5.1 Germanium evaporation

In order to improve the robustness of the residual bridge after the first spin-coating of 470 nm of MMA, the additional layer of 100 nm Ge was added. It was deposited in the same evaporation set-up (see Fig. 3.3), as the evaporation chamber has 7 different targets with various materials which could be used in the same run. Germanium was evaporated after pre-cooling of the sample in the main chamber for 1 hour at a temperature of about -130 °C. The rotation angle was 183° with a tilt of 7' + 0.15". The source temperature was held at 1375 °C, resulting in an evaporation rate of about $6 - 8$ nm/min. The pressure in the main chamber rose up to $5{\cdot}10^{-8}$ mbar. Warming of the sample was done in the load-lock under nitrogen flow for 25 minutes.

After the spin-coat of 220 nm of PMMA and the conventional procedure of the bake (it was done at 157 °C for 50 min for both spin-coating steps of MMA and PMMA because otherwise ger-

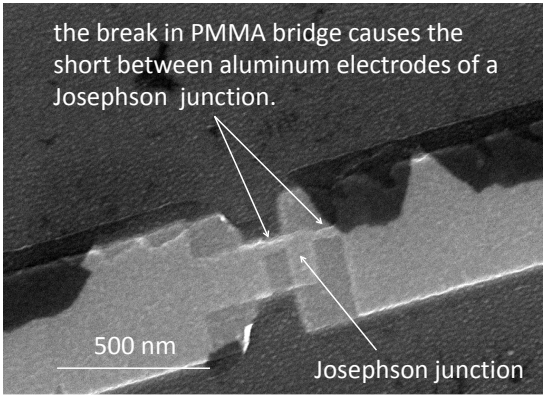

Figure 3.7: The residual PMMA bridge was broken and there is a short from one Al border to the other, sample #2, resonator #3.

manium started to corrugate during the process), the standard lithography step with a reduced dose of $1.3 \times 260\ \mu\mathrm{Cl/s{\cdot}cm^2}$ was held. Then the above described procedure of development was applied.

3.5.2 Germanium reactive ion etching

It is obvious that the standard development procedure will not etch through the hard germanium layer. The lithography step was done as described in Sec. 3.3 and then the development procedure was performed. It transfered the pattern on the upper PMMA resist which is in turn transfered through germanium during the reactive ion etching process (RIE).

The sample was placed in the vacuumed chamber of the RIE machine, and under flow of CHF_3, the germanium layer was etched through the pattern. Then the residual PMMA is etched

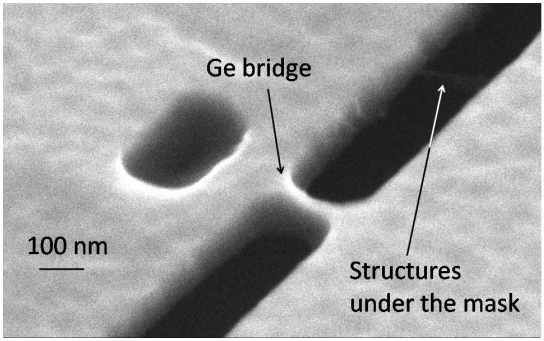

Figure 3.8: The example of an etched Germanium mask.

away in a flow of pure oxygen. The recipe for the flow is 50 sccm CHF_3, 1 sccm O_2 at 140 W and 25 mTorr for the etching of 100 nm of germanium. The time of etching was 8 min 25 s. For oxygen etching the recipe was 10 sccm under a pressure of 100 mTorr, 30 W power and a time of 3 min.

Then the additional development step for the opened MMA sublayer was used. It included placing the sample for 57 s in a mixture of MIBK:IPA with a ratio of 1:3, then in pure IPA for 2 minutes followed by N_2 drying. The SEM picture illustrates an example of the Ge mask patterning, see Fig. 3.8.

At the end the described evaporation procedure is held with the adjustment of the oblique angles to the thickness of Germanium layer. In our case it was a rotation angles of 327 ° with 0.2' + 0.5" and 1' + 0.15" for both aluminum layers.

After the standard lift-off, structures of excellent quality were obtained, see Fig. 3.9.

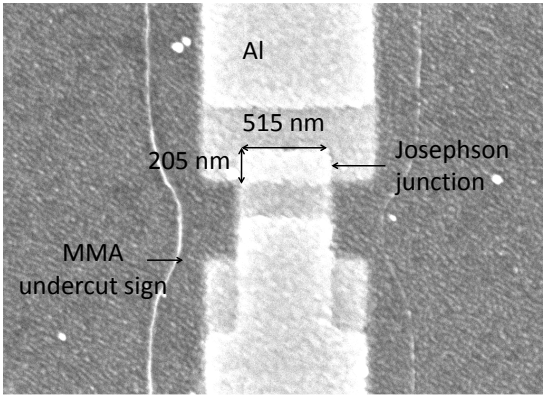

Figure 3.9: The SEM picture of a Josephson junction in a 3 JJ flux qubit fabricated using the Ge mask technique. The corners of the structure are visibly sharper, which is one of the greatest advantages of this process, supporting a more precise qubit α-factor definition, sample #3, resonator #1.

3.6 Fabricated samples

We fabricated a series of hybrid $Al/AlO_x/Al$ Josephson junctions on the Nb contact pads having the dimensions of 0.2 ± 1.0 μm^2 using the technique described above. The directed Ar beam etching was used in order to remove the NbO_x; Ge mask step was not applied.

Flux qubit chips of two kinds were fabricated, their overview is given in Tab. 3.1. Al-based flux qubits (sample #1, see Tab. 3.1) were made in order to characterize the qubit gap spread and represented an Al ring interrupted by 3 Josephson junctions. The Al loop was fabricated directly on the silicon substrate and didn't require the Ar beam etching or the Ge hard-mask technique, thus having a significantly shorter fabrication cycle.

Table 3.1: Summary on fabricated samples.

sample number	1	2	3
type of qubits	Al-based	hybrid Nb/Al	hybrid Nb/Al
Ar cleaning	no	yes	yes
Ge mask used	no	no	yes

The dimensions of JJs in flux qubits were halved, $0.2{\times}0.5\ \mu\mathrm{m}^2$ for the large junctions and the α-junctions aimed α being in the range from 63 % up to 67 %.

Samples #2 and #3 (see Tab. 3.1) contained flux qubits possessing the Nb and Al parts. The Al part had three Josephson junctions as well, whereas Nb part could posses the SFS Josephson junction or be just a Nb strip. In this case the Ar etching was necessary to remove the NbO_x, and for the last measured sample #3 the Ge hard-mask technique was used. Every hybrid chip contained both types of the Nb-Al hybrid qubits, with and without π-junctions, which could be therefore measured in the same cool-down run. Thorough designs of flux qubit chips is presented in Sec. 4.2.1 and Sec. 4.2.2.

3.7 Conclusion

In this chapter, the fabrication process of Al-based as well as Nb-Al hybrid flux qubits with Josephson junctions and π-junctions was described. The challenge was in removing the NbO_x without damaging the PMMA layers. We developed procedure of Ar in-situ etching for this purpose. An additional

technological process included the usage of germanium mask evaporation.

4 Measurement setups

In our experiments two cryostats were used. The Oxford HelioxVL ^{3}He cryostat had a base temperature of 300 mK and was used for characterization of hybrid Nb/Al/AlO_x/Al/Nb junctions. The dilution refrigerator KelvinoxIGZ produced by Oxford Instruments with a cooling power of 100 μW at a temperature of 100 mK, was used for measurements of all flux qubits.

4.1 Measurements of hybrid Nb/Al/AlO_x/Al/Nb junctions

It is important to know the values of critical current densities in Josephson junctions in order to design a flux qubit with required parameters. The flux qubit gap depends on I_c and capacitance of its junctions. To determine I_c current-voltage measurements on test JJs were performed.

After the fabrication process, the sample with test hybrid JJs was mounted onto the sample holder of the Heliox ^{3}He cryostat, shielded with a cryopermalloy shield from fluctuations of the external magnetic field and cooled down to 300 mK.

Several junctions were destroyed before the cool down during the first measurements, presumably due to electrostatic discharge. To prevent this, the Nb pads were shorted before the

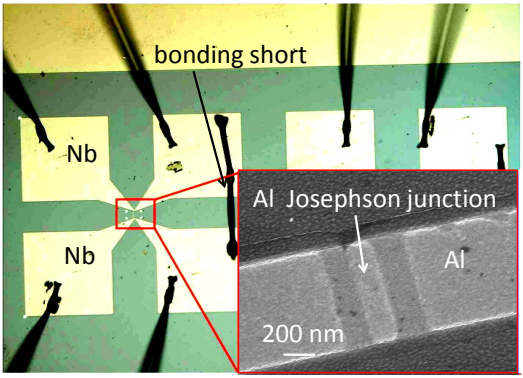

Figure 4.1: Nb pads were fabricated with the help of standard DC magnetron sputtering. The inset shows an Aluminum stripe, a Josephson junction is situated in the middle. A bonding short in parallel to the Josephson junction protects the sample from electrostatic discharge.

bonding of the sample to the sample holder, in order to protect the Josephson junction (Fig. 4.1).

While applying a small bias current, the short was removed manually, and the reference oscilloscope picture showed a voltage jump of the current-voltage characteristic to the expected value of room temperature resistance of the junction. During the whole cool-down, a small current of about 20 nA was leaking through the junction. On one hand, this protected the junction from the electric discharge, and on the other hand, it helped us to avoid the current jump in the first moment of a measurement. With this protection, all other junctions were successfully investigated. Custom-made analog electronics generated the current and acquired the voltage from the sample. The wiring

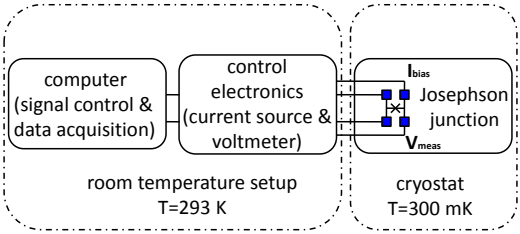

Figure 4.2: Schematic of the experimental setup for measurements of IV characteristics of hybrid Nb/Al/AlOx/Al/Nb Josephson junctions.

consisted of a set-up of twisted pairs, their quantity was defined by the number of junctions on the chip. The IV curves were measured using a four-point configuration. The measurements were controlled by a computer using a National Instruments interface and a DAC custom-made analog module. The general scheme of measurements of hybrid JJs is presented in Fig. 4.2.

4.2 Measurements of flux qubits

A frequency-selective readout scheme for several superconducting qubits, which are placed near individual $\lambda/4$-resonators which, in turn, are coupled to the same microwave transmission line, opens the way to scale qubit circuits up without increasing the number of measurement lines [13, 53]. If we use a flux qubit with a π-junction in this scheme, theoretically, we would be able to shift the working point from $\Phi_0/2$ to 0 without applying

external flux bias [54], thus minimizing the flux noise in the qubit loop and improving its coherence time. Additionally, the possibility of placing several flux qubits with different thickness of the ferromagnetic layer in an SFS-junction would give the possibility to increase the scheme scalability, performing the readout of several distinguishable flux qubits using a single transmission line and a single resonator.

We started from fabrication and measurements of flux qubits consisting of an Al ring interrupted by three Josephson junctions. These were made in order to test the quality of our Al junctions and the technological process, as well as to find out the qubit gap. Furthermore, as satisfactory results were achieved, the next step was performed, which included fabrication and measurements of Nb/Al hybrid flux qubits with and without π-junctions, named hybrid π-qubits and 0 qubits, respectively.

4.2.1 Design of Al-based flux qubits with 3 Josephson junctions

The flux qubit measurements presented in this thesis were performed on several chips, using the dispersive readout measurement scheme for flux qubits with different α-factors. The design and detailed characteristics of the resonator layout are presented in [53] and [13], here we will describe them in brief.

The chips were 5×10 mm^2 large and included 7 coplanar waveguide $\lambda/4$-resonators with a corresponding geometrical length from 2762 to 2462 μm in steps of 50 μm (10J-SPMJ5). The corresponding resonance frequencies were estimated to range from 10.640 GHz for the longest resonator up to 11.72 GHz for the shortest one, in steps of approximately 180 MHz. The resonators were capacitively coupled to a transmission

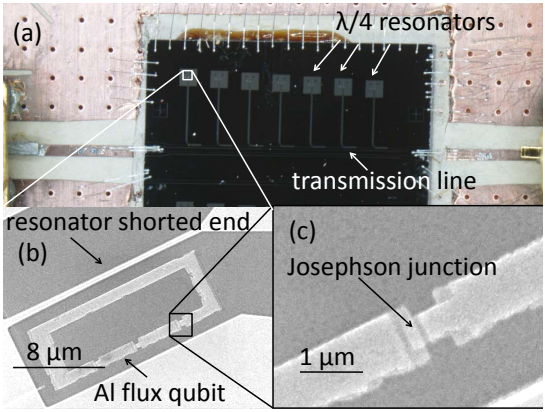

Figure 4.3: Micrograph of a sample #1 with Al flux qubits. a) The complete chip. Seven $\lambda/4$-resonators are capacitively coupled to a transmission line with an elbow resonator open end. The white square outlines the location of an Al flux qubit. b) The Al flux qubit interrupted by three Josephson junctions is situated near the shorted end of the resonator and thus inductively couples to it. The black square marks the area of a large JJ. The α-factor is designed to be in the range from 67% to 69% in steps of 0.4%. c) The large Josephson junction had an area of about 0.2×0.5 μm^2.

line using elbow couplers. The coupling strength was chosen to result in an external quality factor of ≈ 1500. The inner conductor of each resonator had a width of W=20 μm, the gap between the central strip and the ground was G=11 μm. At the shorted end the resonators were narrowed to W=1 μm and had G=8 μm, where Al flux qubits were placed.

Six Al-based flux qubits were situated near the six longest resonators, one was left for reference measurements. Flux qubits had a loop area of 4×12 μm^2 and α-factor variation from 67% to 69% in steps of 0.4%. The critical currents of the large Joseph-

son junctions were supposed to be around 1.57 μA, resulting in a corresponding persistent current I_p around 1 μA, giving an estimated qubit gap in the range of 1.96 to 3.39 GHz and estimated bare coupling of 128 MHz. The qubits were galvanically decoupled from the resonators. Traps for Abrikosov vortices [55] of size 10×10 μm^2 surround the shorted resonator ends, as can be seen in Fig. 4.3 (a). The detailed view of the sample is presented in Figs. 4.3 (a,b,c). The measurement results of the samples will be discussed in Chap. 5.

4.2.2 Design of Nb/Al hybrid 0- and π-qubits

After the successful measurements of spectroscopy plots of Al flux qubits (see Sec. 5.3), the design with Nb/Al hybrid 0- and π-qubits were created. There were a few major changes in the design in comparison to the design of Al-based flux qubits:

1. Three chips with the dispersive readout scheme were situated on every substrate 12×12 mm^2 large, with the resonator shorted ends directed to the center of the substrate. They differ from each other by the SFS areas, which were 8×8 μm^2, 10×10 μm^2 and 14×14 μm^2 large.

2. The forth corner of the chip was occupied by a test π-junction. As it was mentioned in Chap. 3, the technological process could affect the thickness of the ferromagnetic layer of the π-junction, thus leading to a $\pi \rightarrow 0$ transition. The critical currents of the test π-junctions were determined after the low-temperature measurements of flux qubits in the dilution refrigerator.

3. The resonators were squeezed closer to the center of the substrate. This was a requirement of the π-junction technology

Table 4.1: Characteristics of hybrid qubits on the sample #2.

resonator	#1		#2	#3	#4	#5	#6	#7
qubit type	π	0	π	π	π[1]	0	0	no
contain SFS	yes	no	yes	yes	yes	no	no	no
contain SiO_x	yes	yes	yes	yes	yes	yes	no	no

[1] The forth resonator is shorted to the ground through the π-junction, see Fig. 4.5, (c).

(see Chap. 3). The CuNi thickness was supposed to be uniform in the middle circle of the substrate with a diameter of 3-4 mm.

4. A resonator shorted to the ground through the π-junction was added in order to investigate the noise which could be added to the system by a π-junction.

5. Nb pads for hybrid Josephson junctions were designed on every chip. Measurements of hybrid JJs will be discussed in Sec. 4.1.

Let us now consider the design of the chips in details.

The chips were 6.3×6.3 mm^2 large, and included 7 coplanar waveguide $\lambda/4$-resonators with a corresponding geometrical length from 2764 to 2414 μm. At the shorted end the resonators were narrowed to W=2 μm. The overview of the structures, situated near each resonator, is presented in Tab. 4.1.

The longest three resonators had lengths from 2764 to 2664 μm in steps of 50 μm. Near the shorted end of the first resonator two flux qubits with and without integrated SFS $Cu_{0.47}Ni_{0.53}$ π-junction were placed (π- and 0-qubits), opposite to each other in their own gap (see Fig. 4.4). The gaps increased their area up to 37.5×50 μm^2 and 39.5×50 μm^2, respectively, because of

the Nb part size requirements. The alignment in the optical lithography process in Russia had a precision of about 3 μm. In addition, the Al part could be attached only to the bottom Nb layer, which was structured by RIE and thus had a smooth edge. All this restrictions led to a size of 20×45 μm^2 of the Nb qubit part. The loop area was designed to be equal for both qubits, but the distance to the shorted end was 1 μm for the π-qubit and 2 μm for the 0-qubit. This led to 10 GHz and 8 GHz of expected bare coupling energy (2.39) for each qubit, respectively. The aluminum part of the flux qubits was interrupted by three Josephson junctions, one α times smaller than the other two.

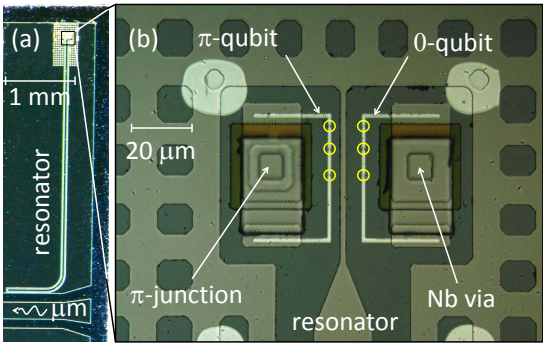

Figure 4.4: a) $\lambda/4$ resonator capacitively coupled to a transmission line. b) Optical picture of two hybrid Nb/Al flux qubits placed near the shorted end of the longest $\lambda/4$ resonator. The Nb part of the left qubit contains an SFS $Cu_{0.47}Ni_{0.53}$ π-junction. The right qubit has a Nb "via" structure forming a superconducting short. The circles mark the positions of the aluminum Josephson junctions.

The second and the third resonator contained a single π-qubit. The forth resonator didn't contain any qubit, but was shorted to the ground through a π-junction, see Fig. 4.5, (c). Its length was 100 μm less than that of the third resonator, in order to take into account a shift of the resonant frequency implied by a π-junction, discovered by Fengbin Song (private communication).

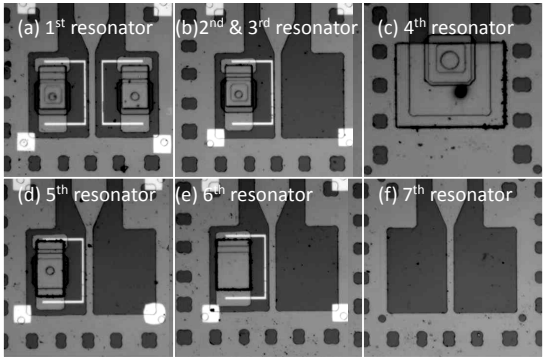

Figure 4.5: Micrograph of the shorted ends of all resonators on the sample #2. The holes in the ground play the role of flux traps. a) The first (longest) resonator with 0- and π-qubits. The 0-qubit had the SiO_x spacer between the top and bottom Nb layers. b) The second and the third resonator contained a single π-qubit. c) The forth resonator was shorted through a π-junction to the ground plane. d)The fifth resonator had a 0-qubit with the SiO_x spacer between the top and bottom Nb layers. e) The sixth resonator with a 0-flux qubit, which didn't contain the SiO_x spacer. f) The seventh resonator was left empty for reference measurements.

The fifth resonator had a qubit with both the Nb part and the SiO_x spacer, but without a ferromagnetic layer. This qubit

was intended to be compared with the π-qubits in order to see, whether the CuNi integration resulted in additional noise in the system. The qubit near the sixth resonator contained only the Nb film as the Nb part, in order to make the same conclusions about the spacing SiO_x layer. The seventh resonator gap didn't contain any Nb part, such that it was possible to leave it empty or to put an Al flux qubit for reference measurements.

The large Al JJs of all qubits had an area of about 0.2×0.5 μm^2. The designed variation in α-factor from 69 % to 71 % in steps of 0.4 %. Due to the oxidation conditions in our evaporation set-up, see Sec. 3.3 the critical current of the large Josephson junctions was about 1 μA. Their capacitance was estimated to be C=4.43 fF. The qubit gap Δ was estimated to be in the range of 2.3-3.5 GHz. All realized types of structures placed in the gaps near the shorted resonator ends are shown in Fig. 4.5.

It is well-known that a fabrication process always leaves an uncertainty in parameters, and the experimental curve is the only instance to prove real qubit characteristics.

The Al-based and hybrid qubit chips were measured in the same dilution refrigerator with the same wiring and filtering scheme. The obtained data will be described in detail below.

4.2.3 Sample holders

In order to fix the sample in the setup and for wiring to measurement electronics, different kinds of sample holders are used. They contain a PCB with planar dc copper wiring. The chip was glued with a low-temperature varnish. For measurements of IV-characteristics we used sample-holders with 24 Cu pads and wires arranged further in twisted pairs going to the room-temperature tunnel electronics as illustrated in Fig. 4.2. For

the qubit measurements, SMB microwave connectors were soldered on a PCB. These sample holders represent a box, with the sample placed inside. Microwave cables are attached through the upper side of the box, which contains also a hole to insert a low-inductance coil (named further the fast coil) for qubit spectroscopy measurements, as shown in Fig. 4.7.

The inner part of the box is covered by epoxy mixed with copper powder in order to reduce the reflection of microwaves inside the box, therefore damping parasitic resonances of the sample-holder. This is important for qubit measurements, as the resonances are tending to couple directly to the qubit, reducing its coherence time and smear the spectra.

The sample holder box is surrounded by the flux-bias coil. It consists of 1500 windings of the NbTi wire, which becomes superconducting at a temperature of about 9 K.

Bonding

To connect the chip with the measurement set-up we used IPT HB06 ultrasonic wire bonding machine. The sample holder and the transmission line were galvanically connected with 25μm wide aluminum wires using the ultrasonic welding technique. We also needed to connect the ground plane of the chip with the ground of the sample holder in order to avoid parasitic potentials. In order to lower the bond inductance, thus avoiding an impedance mismatch between the transmission line of the chip and the sample holder several wires were bonded to the transmission line. The chip placed in the sample-holder and ready for measurements is depicted in Fig. 4.6.

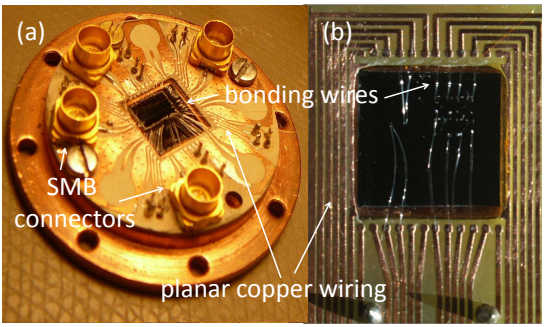

Figure 4.6: a) A sample bonded to the sample holder for the Oxford Instruments KelvinoxIGZ dilution refrigerator. b) A sample bonded to the sample holder of the Oxford HelioxVL ^{3}He cryostat.

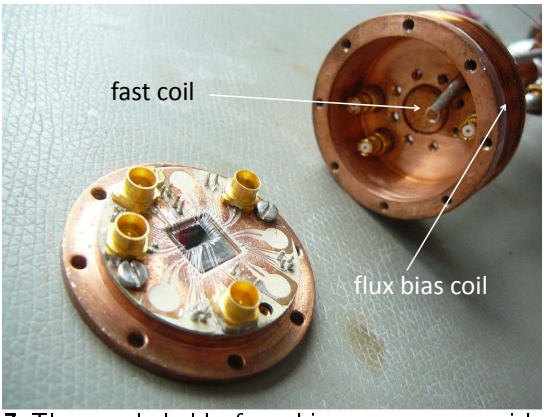

Figure 4.7: The sample-holder for qubit measurements with a sample. It is possible to see the fast coil for spectroscopy measurements, inserted through a hole in the upper side of the housing.

Magnetic shields

Flux qubit measurements are very sensitive to any external magnetic noise. Unfortunately, the environment always provides it, for example, the earth magnetic field, magnetic field fluctuations from pumps and neighboring setups, etc. In order to reduce their impact the sample holder box is placed in a superconducting lead shield and then in a μ-metal cryoperm shield (see Fig. 4.8, (b)).

4.2.4 Microwave measurements

The dispersive readout is based on the fact that due to the coupling to its dedicated qubit, each resonator acquires a resonance frequency shift depending on the state of the qubit, see 2.52:

$$\Delta\omega_r = \pm\frac{\tilde{g}^2}{\omega_q - \omega_r}, \tag{4.1}$$

where $\tilde{g}$ is the effective coupling of the resonator to the flux qubit, ω_q is the transition frequency between the $|0\rangle$ and $|1\rangle$ qubit states, and ω_r is the resonance frequency of the unperturbed resonator. From (4.1) we see that when the qubit is far-detuned from the resonator frequency $\omega_q \gg \omega_r$, the dispersive shift is small. When the qubit frequency approaches the one of the resonator, a relatively large dispersive shift $\Delta\omega_r$ occurs.

It is also important that resonators have high quality factors, resulting in clearly indistinguishable resonance curves.

4.2.5 Dilution refrigerator and microwave equipment

In order to reach even lower temperatures than 300 mK, one has to use more complex methods. The most known way is used in current dilution refrigerator setups based on the properties of ^{3}He/^{4}He mixture. After being cooled down to 870 mK, the mixture separates to a ^{3}He-rich phase (the concentrated phase) and a ^{3}He-poor phase (the dilute phase). At very low temperatures the rich phase consists only of ^{3}He, while the dilute phase has approximately 6.6 % of ^{3}He and 93.4 % of ^{4}He. In the mixing chamber two phases are separated by a phase boundary, and ^{3}He from the rich phase dilutes adiabatically into the dilute phase. This is an endothermic process and it removes the heat from the mixing chamber environment. The heat needed for this process provides the useful cooling power of the refrigerator. This technique was proposed by Heinz London in early 1950th and allowed one to reach temperatures down to 2 mK.

For the low-temperature measurements of our qubits we used the dilution refrigerator KelvinoxIGZ produced by Oxford Instruments with a cooling power of 100 μW at a temperature of 100 mK. For the application of a microwave signal we used a commercial Anritsu VectorStar MS4642A network analyzer (VNA) [56], designed to measure continuous wave signals between 70 kHz and 40 GHz transmitted through and reflected from a device. The overview of the experimental setup and magnetic shielding is presented in Fig. 4.8.

The room temperature readout scheme is shown in Fig. 4.9. The idea and technical realization of the setup was performed by Marcus Jerger and Stefano Poletto, being described in detail in [53, 13]. Here we present it in brief. The wiring consisted of

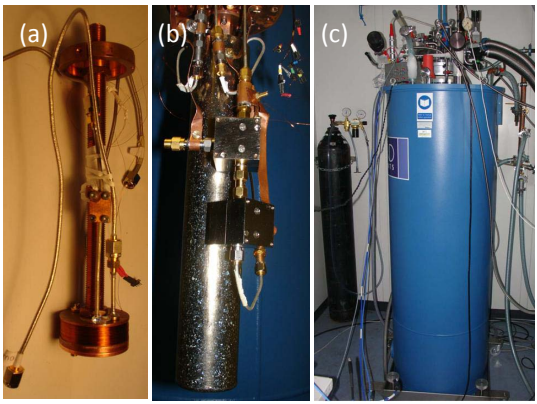

Figure 4.8: a) The sample-holder box prepared for attaching to the dilution fridge. b) Magnetic shielding of the sample-holder and the wiring with two circulators. c) Dilution refrigerator overview.

input and output microwave cables (to and from the delution refrigerator), connected to the transmission line of the sample, and a set of low-frequency twisted pairs, one of which was used for the flux bias coil. The signal from the qubit was picked up by a low-loss Nb cable and amplified by a broadband cryogenic amplifier LNF6-20, thermally anchored to the 4.2 K stage. The measurements were performed at a temperature of $T \approx 25$ mK. For field response measurements we swept electrical current through the bias coil, thus changing the magnetic flux through the qubit loop. At the same time we probed the $\lambda/4$ resonator frequency ω_r with a microwave signal from the VNA.

In order to reconstruct the qubit parameters, frequency spectroscopy measurements were carried out. Two microwave signals were applied to the feed line. One excited the qubit and

thereby changed the dispersive shift of the resonator frequency, and another weakly probed the resonator frequency.

Amplification and filtering inside the dilution refrigerator

As already mentioned above, the flux qubit measurements are very vulnerable to external noise, including thermal and electromagnetic noise. That is why several filters and amplifiers were placed inside the dilution refrigerator, for the essential information about the setup see [53] and [13].

In the input line, which feeds the transmission line of the sample, 3 attenuators of 20 dBm each were placed on the 4.2 K and 30 mK plates. Our input coaxial cables were made from stainless steel, which provided another 10 dB.

For the output line due to the very weak qubit signal we couldn't use attenuators, but we still needed to protect the sample from thermal noise which could come through the cable from the higher temperature stages. That is why circulators were used - the signal from the qubit passed without attenuation, but for the other way around they supply isolation of several tens of dB in the required frequency range.

We had three circulators in our output line. Two Pamtech XTE1238K cryogenic circulators for 8-12 GHz frequency range were placed right after the sample at the 30 mK plate and gave an isolation of 20 dB each. The Mini-Circuits VHF-8400+ bandpass filter for 8-12 GHz frequency range was installed right after the circulator chain. The third circulator was placed on the 4.2 K stage, had 8-18 GHz frequency range and 20 dB of isolation. For increasing the useful signal/noise ratio a cryogenic HEMT amplifier at the 4.2 K stage was used, giving a gain of 26 dB.

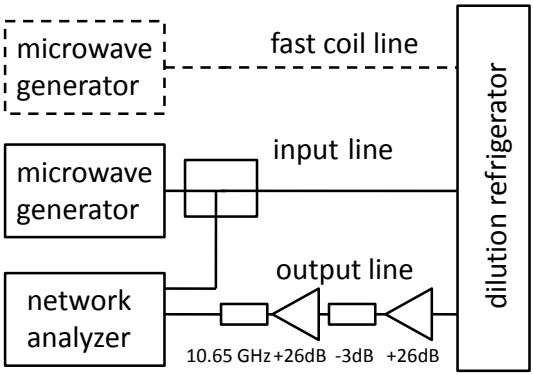

Figure 4.9: Schematic picture of the room-temperature measurement scheme. There are two room-temperature amplifiers with a gain of +26 dB each and a filter for 6.3-15 GHz frequency range placed right before the network analyzer. The attenuation of -3 dB between the amplifiers serves to damp reflections of microwave signals in the wire. The flux qubit excitation signal from the microwave generator can be applied in two ways: directly through the transmission line, the correspondent schematic part is shown by the continuous line, and through the fast coil line, shown by the dashed line. The input line is a stainless steel line, which is not superconducting. It adds additional attenuation of the thermal noise, which can enter from the upper stages. The output line is made from a superconducting CuNb wire, which doesn't damp the qubit signal. The input fast coil line is also made from CuNb, but the coupling of the fast coil is so weak that fluctuations in it don't disturb the qubit. At the network analyzer ports dc-breaks are installed in order to filter low-frequency noise components. The network analyzer has a range of ± 20 dB attenuation/gain, which can be used for fine power tuning. The reflections in the wiring were suppressed by adding 1 dB attenuators between the circulator and VNA in the output line.

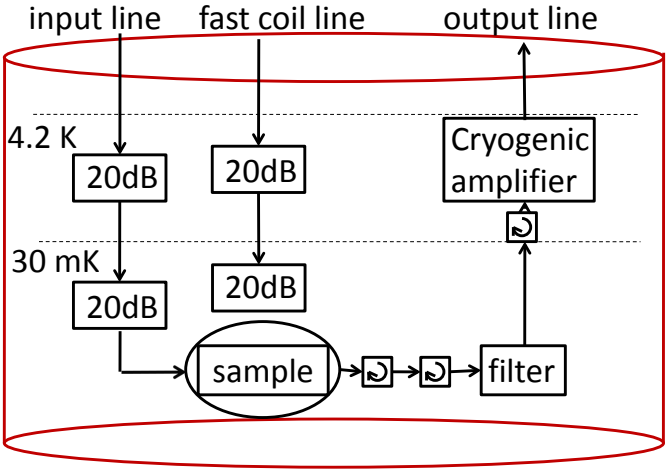

Figure 4.10: Wiring and filtering inside the dilution refrigerator, [53]. Attenuators, circulators and cryogenic amplifier are placed on the 4.2 K and 30 mK plates.

The fast-coil line was also supplied by two 20 dB attenuators on the 30 mK and 4.2 K plates, although its coupling to the sample is small.

Noise in the flux-bias coil was reduced by LC low-pass filters placed at 1.6 K temperature. The wiring inside the cryostat is shown in Fig. 4.10. A circled arrow in a box represents a circulator.

Data acquisition

During the measurements, a computer controlled the microwave generator, the network analyzer and the tunnel electronics, as

well as received the data through a GPIB interface. Python software was developed by Markus Jerger [53] especially for flux qubit stationary and time-domain measurements, giving the possibility to observe measurements in progress. For fitting operations and a background calibration of color-coded resonator's signal plots vs. both coil current and frequency the MATLAB environment was used.

5 Experimental results and their discussion

5.1 Characterization of hybrid Josephson junctions

Characterization of the hybrid Nb/Al/AlO_x/Al/Nb Josephson junctions with different times of Ar beam NbO_x etching gave interesting results. The first attempts of NbO_x removal were performed with the Ar beam etching during 1 minute and accelerating beam voltage of about 1kV. The IV characteristics showed the presence of the residual NbO_x, they had additional features at a linear combination of superconducting gap voltages of Nb and Al, discussed for similar structures in [57] and [58] (see Fig. 5.1).

For the developed Ar etching procedure, the current-voltage curves were identical to common Al/AlO_x/Al Josephson junction IV characteristics (see Fig. 5.2), thus showing no evidence of the Nb/NbO_x/Al interface.

Switching current values of $I_s = 2 \pm 0.54\mu$A and re-trapping currents of around $I_t = 1\pm\ 0.25\ \mu$A were measured for junctions, fabricated on several chips. From the area of the junctions we could estimate the corresponding junction capacitance $C \approx 8.8 \pm 1.8$ fF. The pronounced back-bending of the re-trapping current branch visible in Fig. 5.2 is rather typical

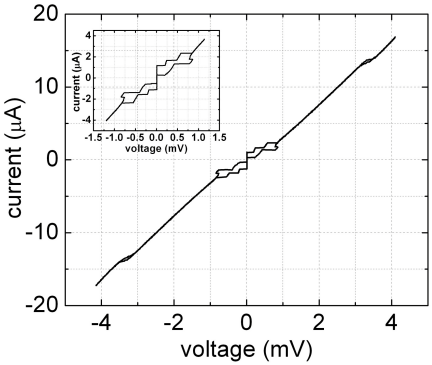

Figure 5.1: Current-voltage characteristics of a hybrid Nb/Al/AlO$_x$/Al/Nb Josephson junction made using the Ar etching time of 60 s and an accelerating voltage U=1 kV. The inset shows a zoom in hysteresis of IV around V=0 mV.

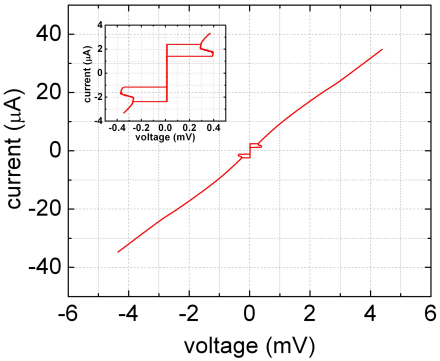

Figure 5.2: A typical current-voltage characteristic of a hybrid Nb/Al/AlO$_x$/Al/Nb Josephson junction made using the developed Ar etching procedure, see Chap. 3. Re-trapping current back-bending is explained by the self-heating of the junction.

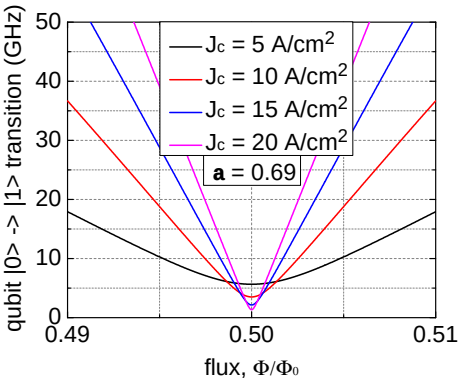

Figure 5.3: Estimated flux qubit gap variation versus a normalized flux bias for different critical currents of a Josephson junction. Qubit parameters are chosen to be in accord with designed parameters of the hybrid π-qubit for the sample #1, resonator #1, discussed in Sec. 5.4: α=0.69 and E_c=2.9·10^{-24} J.

for vacuum-based transport measurements of sub-micron aluminum junctions of high critical current density and can be explained by non-equilibrium effects due to the junction self-heating. This self-heating is also responsible for about 20% reduction in the measured value of the gap voltage V_g [59].

Zooming the IV curves, one can see a small nonlinearity at a voltage range corresponding to the double gap of Nb. This feature is poorly pronounced and will not affect relevant characteristics of Josephson junctions (Fig. 5.2).

The expected variation of a flux qubit gap versus the critical current density of Josephson junctions is illustrated in Fig. 5.3 and Tab. 5.1. The critical current of the Josephson junction I_c depends exponentially on the inverted barrier thickness 1/d

Table 5.1: Qubit gap frequency for different supercurrents.

Supercurrent I_c, nA	E_c/E_J	Qubit gap frequency Δ, GHz
500	0.0175	5.65
1000	0.0088	3.53
1500	0.0059	2.17
2000	0.0044	1.35

[60], while the Josephson junction capacitance $C \sim 1/d$. Therefore small changes of d cause the strong variation of I_c, but rather small variation of C. In addition, the AlO_x barrier has a nonuniform thickness [61], which varies from 1 to 2 nm even for a constant pressure of 0.5 mbar, thus defining the uncertainty in the charging energy of Josephson junctions.

One can see, that even with the critical current I_c two times smaller or larger than actual measured value 1 μA, the qubit gap variation should not exceed 4 GHz (see Fig. 5.3 and Tab. 5.1). In these terms, one could say, that the qubit gap Δ is quite robust with respect to the critical current variation.

On the other hand, the dependence of the flux qubit gap on the α-factor is much stronger (see Fig. 5.4 and Tab. 5.2). 10% variation of the α-factor gives a huge difference of 12 GHz in the flux qubit gap value. As mentioned above, 1% of α-factor corresponds in our process to 5 nm of JJ length. For example, 30 nm deviation from 335 nm of the α-junction length can easily occur due to the lift off, thus influencing the flux qubit gap significantly.

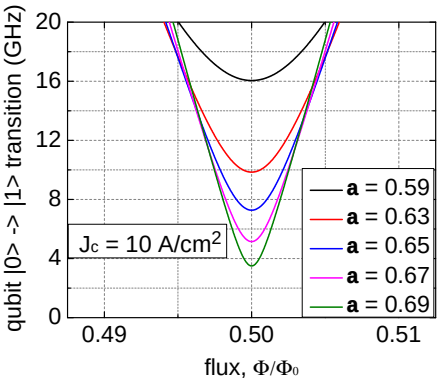

Figure 5.4: Estimated flux qubit gap variation versus normalized flux bias for different α-factors. Qubit parameters are chosen to be in accord with hybrid π-qubit spectroscopy measurements for the sample #1, resonator #1, discussed in Sec. 5.4: I_c=1 μA, E_J=3.3·10^{-22} J and E_c=2.9·10^{-24} J.

5.2 Flux qubits measurements

5.2.1 Readout resonator characterization

The chip characterization starts from measuring the frequencies of the resonators on the chip. They are designed as notch filters, therefore a signal transmitted through the feed line should display several dips vs frequency. A typical Nb resonator, on which the measurements of Al-based flux qubits were performed, displays this kind of dip presented in Fig. 5.5.

In case of the overloaded resonator, its bandwidth is measured at 3 dB power above the minimum of the transmitted signal, and the internal quality factor Q_{int} can be defined as the inverted normalized bandwidth of the resonance curve. The loaded

Table 5.2: Qubit gap frequency for different α-factors.

Supercurrent I_c, nA	α-factor	Qubit gap frequency Δ, GHz
1000	0.59	15.58
1000	0.63	9.85
1000	0.65	7.27
1000	0.67	5.16
1000	0.69	3.5

quality factor Q_{load} can be found as the inverted bandwidth at -3dB power below the unity transmission level, see Fig. 5.5. Therefore, the loss rate to the external circuit or Q_{ext} can be obtained from

$$\frac{1}{Q_{ext}} = \frac{1}{Q_{load}} - \frac{1}{Q_{int}} \tag{5.1}$$

In more general case, Q_{int} is defined as inverted normalized bandwidth at the point where the power dissipated on the internal resistor is halved in comparison to the resonance point. The loaded quality factor is determined at the point, where the reactance of the resonator is equal to the sum of the internal and external resistance. The detailed derivation of Q_{int} and Q_{ext} using equivalent circuit and scattering matrix approaches can be found in [62] and [63].

5.2.2 Working point calibration

In order to perform dispersive measurements, we set the frequency close the resonator frequency and sweep the current of

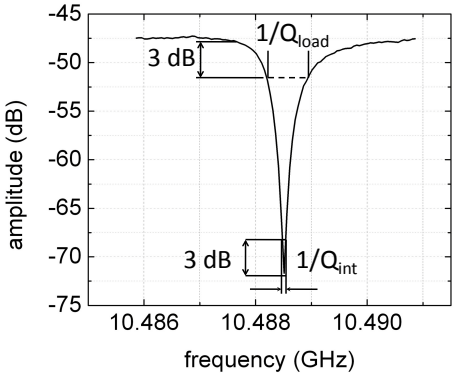

Figure 5.5: Resonator measurements for quality factor estimations, the sample #1, resonator #1 with f_r=10.4885 GHz.

the flux bias coil. It was discussed in Sec. 2.5.3, that the dispersive shift of the bare resonator frequency is dependent on the detuning of the flux qubit frequency from resonator frequency $\omega_{rq} = \omega_r - \omega_q$, see equation (2.52). The qubit is far detuned from the resonator for all flux bias values except a few mΦ_0 around the $\Phi_0/2$ point. At this point, as the dispersive shift is proportional to ω_{rq}^{-1}, at zero flux bias we observe the bare resonator frequencies. Thus, if we set the network analyzer frequency to the bare resonator frequency and sweep the flux bias, we should be able to distinguish a flux qubit state, encoded in the phase and amplitude of the transmitted signal.

As a result of the Φ_0-periodic behavior of the flux qubit transition frequency, (see Fig. 2.7), we obtain a periodic magnetic field response of a dispersive shift of the resonator (see Fig. 5.6). From this graph one can estimate a coil bias current ΔI, corresponding to one magnetic flux quantum Φ_0 penetrating the

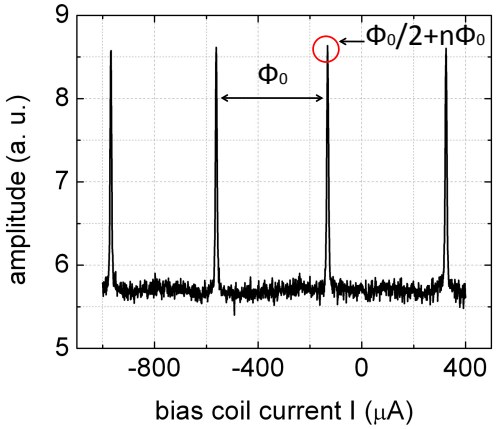

Figure 5.6: Example of the field response of the flux qubit. The data are obtained for the sample #2, resonator #5 fixed at the resonance frequency of f_r=10.4885 GHz.

qubit loop. For this particular sample and resonator, we found $\Delta I = 457\ \mu$A. Further one of the peaks of the field response is chosen and zoomed in. If the qubit gap frequency Δ is smaller, than the resonator frequency $\omega_r/2\pi$, the peak is doubled (see Fig. 5.7). In this case, two peaks mark the places, where a flux qubit energy level splitting equals to the resonator frequency as it is described by equation $\omega_q = \sqrt{\Delta^2 + \epsilon^2}$ (see Fig. 5.7).

If the measurements are done at microwave powers high enough to populate the higher resonator levels, we should be able to see high-order transitions in Jaynes-Cummings Hamiltonian (2.41) discussed, for example, in Refs. [53], [64] and [65]. This could give an understanding of side peaks near the avoided level crossing peaks in Fig. 5.7. However, the spectroscopy of the qubit in Fig. 5.10 shows some strange unexplained

resonances, marked by black dashed lines, appearing at the constant magnetic field, which could be also a reason for the side peaks.

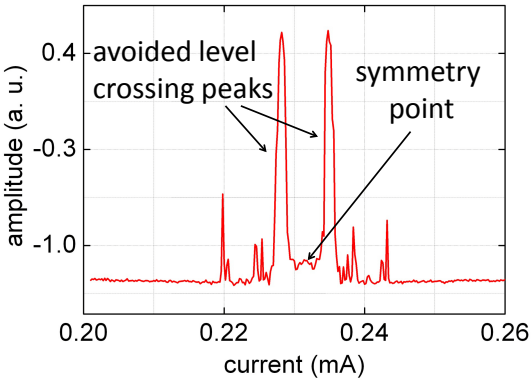

Figure 5.7: Zoom in the double peak of the field response, sample #1, resonator #1 with f_r=10.4885 GHz.

If there is just a single field response peak, the qubit gap frequency is higher than the resonator frequency, unless the resonator dip is too shallow (its quality factor is too low) to resolve the avoided level crossing peaks. Thus, if the quality factor of a resonator is high, the qubit gap should be higher than the resonator resonance frequency.

5.2.3 Two-tone measurements.

It is possible to directly excite a qubit by applying an additional microwave tone to the feed line (see Sec. 2.3.3). If the frequency of the signal is adjusted to a $|\text{-},\text{n}\rangle \rightarrow |\text{+},\text{n}\rangle$ (see Sec. 2.5.3 and

(2.44)) transition of the Jaynes-Cummings Hamiltonian, we will be able to excite oscillations between the qubit states. This causes the changes of the resonator eigenfrequency with the Raby frequency Ω, thus influencing the phase and the amplitude of the transmitted signal. In principle, higher transitions can be also observed using this method.

The symmetry point of the qubit spectrum is situated between the avoided level crossing peaks. If we now make a frequency scan with the second microwave tone at the symmetry point coil bias current, at some frequency we will see the sign, which corresponds to the qubit symmetry point (see Fig. 5.8).

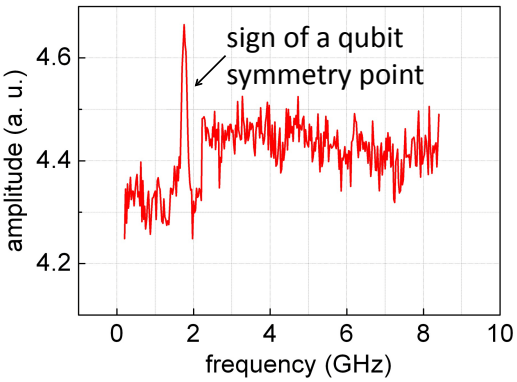

Figure 5.8: A sign of a flux qubit gap Δ on the frequency scan at a symmetry point for sample #1 resonator #1 at f_r=10.4885 GHz and at a symmetry point coil bias current $I_{coil} = 231\ \mu$A.

These three points (two avoided level crossing peaks and a sign of the qubit symmetry point) give us a range for further

Table 5.3: Measured characteristics of resonators, sample #1.

resonator	Resonance frequency, GHz	Quality factor
1	10.488	80680
2	10.671	11600
3	10.866	20502
4	11.058	141775
5	11.262	9640
6	11.492	13416
7	11.723	25501

measurements of color-coded resonator's signal plots vs. both coil current and qubit excitation frequency.

We can thus get the spectroscopy picture, e. g. a flux dependence of the qubit transition frequency, by sweeping a flux bias coil current and a microwave spectroscopy tone frequency.

5.3 Characterization of Al-based flux qubits, sample #1

The technique and setups described above were first used for spectroscopy measurements of flux qubits, which were fully made of aluminum, in order to check the fabrication parameters on a simple system. Resonator frequencies were measured and quality factors were estimated as represented in Tab. 5.3.

Sweeps of coil bias current showed a periodic response for all six resonators. This allowed us to calibrate the coil current per flux quantum ΔI and determine the mutual inductance $M_{q,coil}$ between qubits and the flux bias coil, as summarized in

Tab. 5.4. From the design of the sample we expected that the largest mutual inductance between the flux bias coil and the qubit should occur for the center qubit (qubit #4), because it is situated closest to the symmetry axis of the coil. However, in the presence of the superconducting ground plane the screening currents generate an additional flux bias in the qubit loops thus changing the period of the field response and the qubit-coil mutual inductance [53].

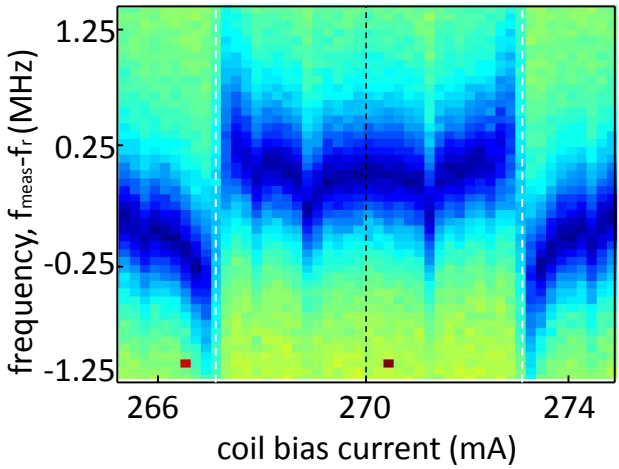

Figure 5.9: Anticrossing measurements at resonator #1 on the sample #1, f_r=10.4885 GHz. Blue color indicates the amplitude response of the resonator in arbitrary units. Black dashed line marks a symmetry point coil bias current. White dashed lines mark the external flux bias, where $\omega_q \to \omega_r$, see Eq. 4.1.

Fig. 5.9 shows the qubit-resonator anticrossings in the transmitted signal for the resonator #1 (color-coded) vs. both coil

Table 5.4: Measured characteristics of Al flux qubits for sample #1.

device	α	$\Delta_{measured}$	$\Delta_{estimated}$	ΔI_{period}	$M_{q,coil}$
1	67 %	2.1 GHz	3.4 GHz	386 μA	5.4 pH
3	67.8 %	$\approx$1.3[1] GHz	2.77 GHz	241 μA	8.6 pH
4	68.2 %	1.6 GHz	2.5 GHz	211 μA	9.8 pH
5	68.6 %	1.0 GHz	2.2 GHz	195 μA	10 pH
6	69 %	0.9 GHz	2.0 GHz	188 μA	11 pH

[1] The gap of the qubit near the third resonator was below the frequency measurement range.

bias current and frequency. The microwave tone probes the frequency of the resonator coupled to the qubit and the resonator shift is expected to occur in agreement with (2.52) from Sec. 2.5.3. In Fig. 5.9 we can clearly see, that indeed the frequency of resonator coupled to the flux qubit changes with the magnetic flux biasing of the qubit, being sensitive to its detuning from the resonator resonance frequency ω_{rq}.

Flux qubit spectroscopy was performed on five resonators. Their properties are summarized in Tab. 5.4. One can see, that the measured gap differs from the designed values, at maximum, by about 1.5 GHz. The larger α-factor is, the smaller are both estimated and measured qubit gaps, as expected from theory in Sec. 2.3.2.

As an example, in Fig. 5.10 the spectroscopy plot of the flux qubit situated near the first resonator is shown. From a fit of the spectroscopy plot of the flux qubit near this resonator it was possible to define the approximate parameters of the qubit: the critical current of the junction $I_c = 1.6 \pm 0.4 \mu$A, the capacitance

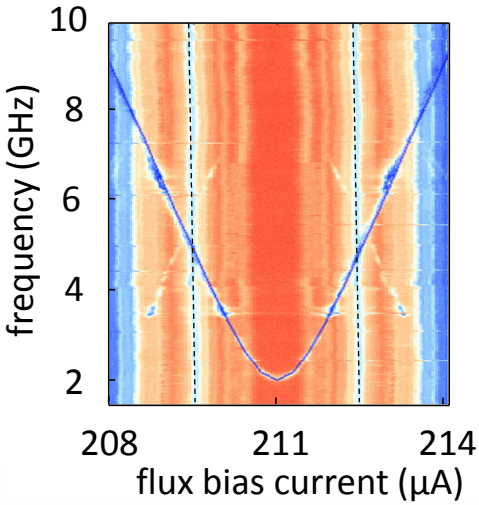

Figure 5.10: Amplitude of the microwave probe tone transmission through the feed line, coupled to the $\lambda/4$ resonator with the flux qubit, sample #1, resonator #1 at f_r=10.488 GHz. Blue color indicates the amplitude response of the resonator in arbitrary units.

of the junction $C = 4.4 \pm 0.9$ fF, fitted $\alpha = 69\%$, which correspond to $E_J = (5.2 \pm 1.2) \cdot 10^{-22}$ J, $E_c = (2.9 \pm 0.6) \cdot 10^{-24}$ J and the qubit gap frequency $\Delta = 2.1$ GHz. The difference between the fitted α-factor, equal to 69%, and the designed one, equal to 67%, can be explained by broadening of the lithography pattern in comparison to the designed one. These values are in agreement with the normal state resistance data from room temperature measurements of test Josephson junctions and STM pictures of the overlap between Al electrodes [61].

The similar Al-based flux qubits were fabricated for fluxon readout measurement scheme, results on their measurements are presented in Refs. [28, 66] and [67].

5.4 Measurements of hybrid Al/Nb flux qubits with and without π-junction, samples #2 and #3

The design of hybrid flux qubits was described in details in Sec. 4.2.2. It was not evident, how the presence of Nb stripe or a π-junction in the flux qubit loop can affect the qubit gap, in most unpleasant case it could be shifted higher than 20 or 40 GHz, where it was difficult to measure the spectrum. Therefore I decided to design the qubit gap even lower than in Al-based flux qubits, aiming for α-factors ranging from 69% to 71% in steps of 0.4%. Two samples were successfully fabricated, see Tab. 3.1 and measured, their measurement results are summarized in Tabs. 5.6 and 5.8.

Sample #2 (see Tab. 3.1) was fabricated with an MMA/PMMA stack without using the Ge mask technique. Partly it had shorts between Josephson α-junction and Al loop of the qubit, which could affect the qubit gap. According to the estimations, a qubit gap could become only lower with increasing of α. This sample was made after just one fabrication cycle, with relatively low baking temperatures of about 130 °C.

Sample #3 was fabricated using an MMA/Ge/PMMA stack and had no shorts. It suffered from several fabrication cycles with up to 10 baking processes with temperatures of about 155 °C, which may have influenced the properties of CuNi layer.

Measurements of sample #2

With this sample, two cool-downs were performed, the second one with improved filtering and an additional circulator. In both cases we measured resonator frequencies and quality factors (see Fig. 5.11). The current of the flux-bias coil was set to zero for the measurement.

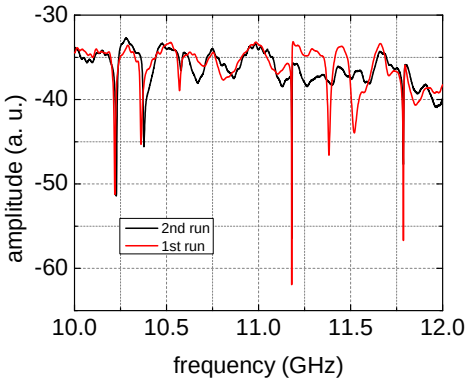

Figure 5.11: Microwave transmission vs frequency for the sample#2 with hybrid Nb/Al flux qubits at zero flux bias for two cool-downs. It is clearly seen that there are only 4 pronounced dips instead of seven for the second cool-down.

In Fig. 5.11, one can see 7 dips with different quality factors, the sharpest two refer to the empty resonator and, perhaps surprisingly, the resonator shorted through a π-junction to the ground. In the second run, shown with the black line, the third, the fifth and the sixth resonator dips became so shallow that it was impossible to distinguish them from the noise. It couldn't happen due to the additional contamination of the sample in the second run, because the sample holder (4.7) was not opened

Table 5.5: Characteristics of resonators for the sample #2, first cool-down.

Resonator	Resonance frequency	Quality factor
1	10.218 GHz	3000
2	10.316 GHz	1300
3	10.569 GHz	550
4	11.177 GHz	10500
5	11.382 GHz	1300
6	11.521 GHz	350
7	11.785 GHz	13250

in the break between these two cool-downs. We just installed an additional circulator in the output line. We believe, that quality factor reduction happened due to Abrikosov vortices, which could be trapped near the resonator. It was investigated in [68], that as the core of the vortex is not superconducting and they move in the presence of microwave field, the dissipation plays an important role, significantly influencing the resonator quality factor. The magnitude of the dissipation depends on the position of the vortices and their amount, and the maximum quality factor reduction observed in [68] for Al resonators was up to 4000.

Unfortunately, the quality factor of the Nb resonators with Nb/Al hybrid flux qubits was rather low. It varied between 350 for the sixth resonator to 3000 for the first resonator with two flux qubits. The detailed information about all resonators is given in Tab. 5.5.

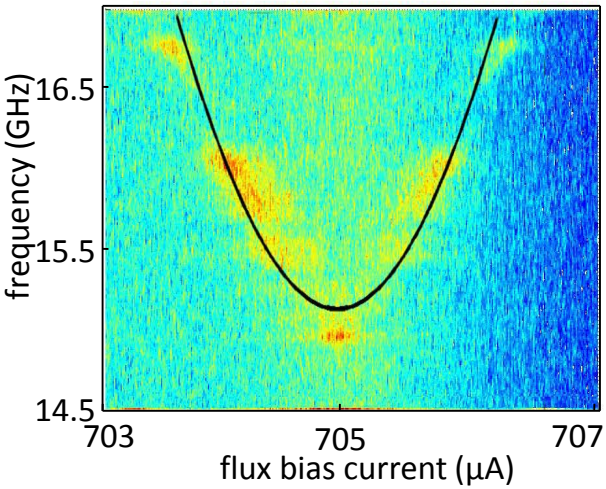

Figure 5.12: Amplitude of a microwave probe tone transmitted through the feed line, coupled to the $\lambda/4$ resonator, sample #2, resonator #1 with f_r=10.218 GHz.

In spite of the bad quality factors, field responses and even spectroscopy lines of several devices were measured. The spectroscopy plots of one of the hybrid qubits situated near the first resonator is depicted in Fig. 5.12.

For fitting curves, a critical current $I_c = 1 \pm 0.3$ μA and a thickness of oxide barrier $d = 2 \pm 0.5$ nm were taken from the IV curves of hybrid Josephson junctions (see Sec. 5.1) and TEM measurements [61], respectively. They resulted in the following values for the two fitting parameters: $E_J = (3.3 \pm 0.9) \cdot 10^{-22}$ J, $E_c = (2.9 \pm 0.6) \cdot 10^{-24}$ J. The fitted α-factor was found to be 59.6 % for the measured qubit gap $\Delta = 14.9$ GHz. It is quite a large deviation from the designed value of $\alpha = 69.4\,\%$ and could,

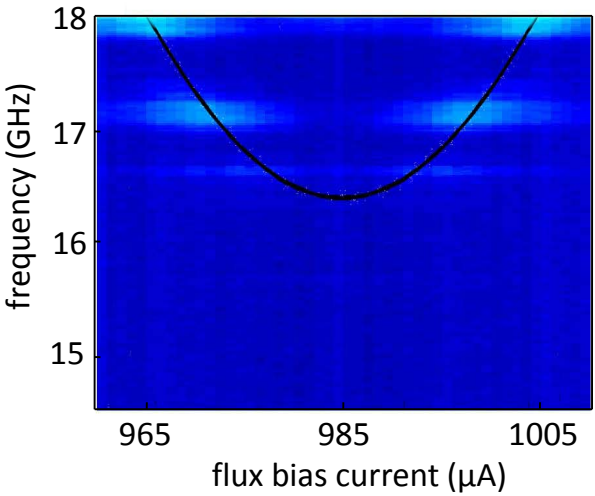

Figure 5.13: Amplitude of a microwave probe tone transmission through the feed line, coupled to the $\lambda/4$ resonator, sample #2, resonator #1 with f_r=10.218 GHz.

most probably, be explained by a variation of the Al Josephson junction area. However, the experiments with Al-based flux qubits showed (see Sec. 5.3), that the technological process can't give such a large spread in flux qubit gap. Therefore the nature of qubit gap value deviation from the expectation stays unclear.

We managed to measure a response from other two hybrid qubits, situated near the first and the second resonator. Both spectroscopy plots are shown on Fig. 5.13 and Fig. 5.14.

Again, there was a large deviation between fitted and designed α-factors. The designed α-factors of hybrid flux qubits with SFS junctions near the first and the second resonators were

69 % and 69.8 %, respectively. The fitting α-factors appeared to be 58.8 % and 60.6 %, respectively.

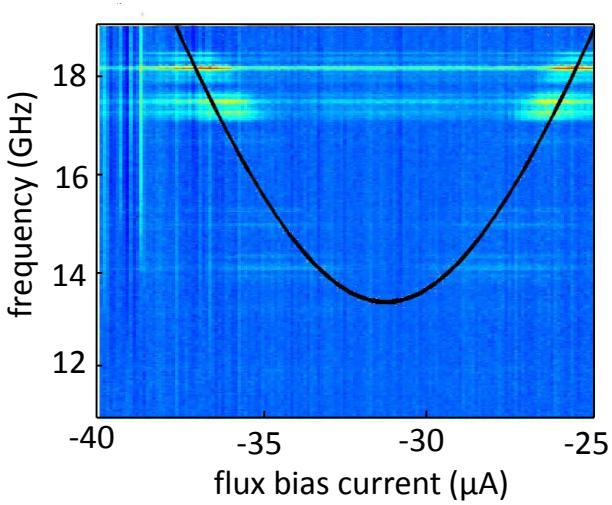

Figure 5.14: Amplitude of microwave probe tone transmission through the feed line, coupled to the $\lambda/4$ resonator, sample #2, resonator #2 with f_r=10.435 GHz.

The fitted parameters of charging energy and Josephson energy were supposed to be the same, as for the hybrid qubit without SFS mesa in Fig. 5.12, being $E_J = (3.3 \pm 0.9) \cdot 10^{-22}$ J, $E_c = (2.9 \pm 0.6) \cdot 10^{-24}$ J because the qubits were done in the same fabrication cycle.

Interesting results were obtained from the measurements of qubits with and without SFS mesas near the first resonator.

We do not name them 0- or π-qubits at the moment because under some conditions which will be discussed later π- to 0-

junction transition can occur. One can easily identify two periods in the field response in Fig. 5.15.

The field response of the resonator, coupled to both qubits is shown in Fig. 5.15. A peak in the transmitted microwave amplitude occurs when the frequency of one of the qubits ω_{q1} or ω_{q2} approaches the resonator frequency ω_r, what happens at a value of the magnetic flux close to $\Phi_0/2 \pm n\Phi_0$ for the qubit without π-junction and at a value of $\pm n\Phi_0$ for the qubit with π-junction, where n is an integer. One can easily identify two periods in the field response in Fig. 5.15.

We suppose that the stronger sensitivity of the qubit with SFS mesa to the applied magnetic field can be associated with an additional Josephson inductance of its loop induced by the π-junction. The amplitudes of the signals from two qubits are referred to the despersive shift of the resonator, as was described in (2.52) and can be different due to their different coupling strengths $\tilde{g_1}$ and $\tilde{g_2}$ to the resonator and the detuning of the qubit gap frequency from the resonator frequency. The energy gap of a flux qubit is extremely hard to control due to its very sensitive dependence on the relation between critical currents for three aluminum junctions. For example, in our experiment for the ratio in amplitudes of signals equal to 0.5 we obtain the corresponding difference in α=2 %, what for our experiments refers to 10 nm of the α-junction length. Such α-factor deviations can easily occur during the fabrication process. The peaks are single, what gives us the possibility to conclude, that the flux qubit gap is higher than the resonator frequency.

As was described in Sec. 3.2, the fabrication process of aluminium flux qubits on a Nb π-junction can influence the properties of the latter a lot. At high temperatures Cu atoms from the CuNi ferromagnetic layer are tending to migrate in

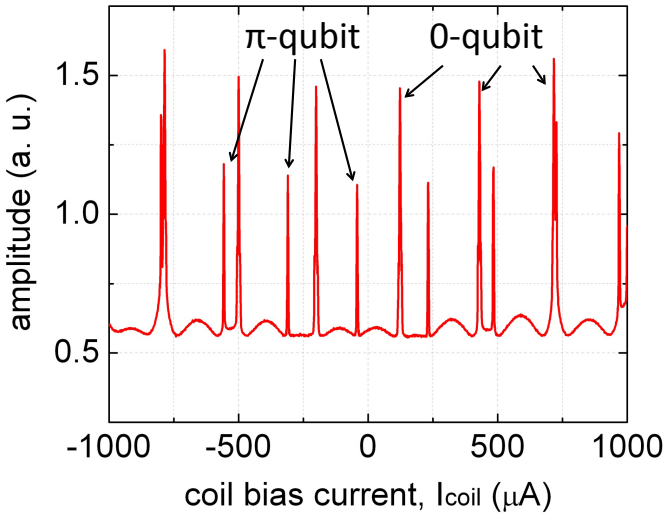

Figure 5.15: Amplitude response of a probe signal through a transmission line at a fixed frequency $\omega = \omega_r = 10.218$ GHz, sample #2, resonator #1. One periodic pattern corresponds to the flux qubit without SFS mesa, another one to the flux qubit with SFS mesa. The difference in amplitudes of the signals can be attributed to the different coupling of the qubits to the resonator and to the different detuning of the qubit gap frequency from the resonator frequency. At the point around $I_{coil} = 700\,\mu$A peaks of both qubits are overlapping, giving the possibility to measure the spectroscopy plot of both qubits simultaneously.

the Nb electrodes, thus reducing the thickness of the layer. The phase shift in the loop depends on the thickness of the ferromagnetic layer in the juntion, and the π-junction can transit to the 0-junction if the changes are crucial [16]. As a result, one of the most important tasks was to determine whether a junction does really give the π-shift or not.

Let us now sort out two families of periodic peaks in Fig. 5.15. This procedure is not straightforward because of non-ideal magnetic shielding. Indeed, one can see from Fig. 5.15 that there is no peak exactly at zero magnetic field, indicating the presence of residual magnetic field in the setup. In Figure 5.16, we have plotted the positions of peaks as a function of magnetic flux. We assumed that a period for each peak family is one flux quantum, the residual flux of less than one flux quantum and the nearest-to-zero peak as corresponding to the qubit with the π-junction. One can see that both peak families could be approximated by linear dependencies, each has its own slope, and their intersection matches to correspond zero total magnetic field. At intersection point we have zero magnetic flux and a π-qubit peak. This makes the peak definition self-consistent and assigns the peak family with smaller flux bias period and amplitude to the flux qubit with SFS mesa and we name it a π-qubit.

After an estimation of the errors we get the position of the crossing point $n_c = 3,438 \pm 0.084\,\Phi_0$ being offset from the peak of the π-qubit by $\Delta\Phi^{\pi} = 0.43 \pm 0.08$ [69].

We cannot completely rule out a possibility, that we can mistake with the relation of π-qubit to the peaks with smaller amplitude. In our samples (see Sec. 4.4) the qubit with SFS mesa is situated closer to the shorted resonator end for resonator #1, thus providing stronger inductive coupling to

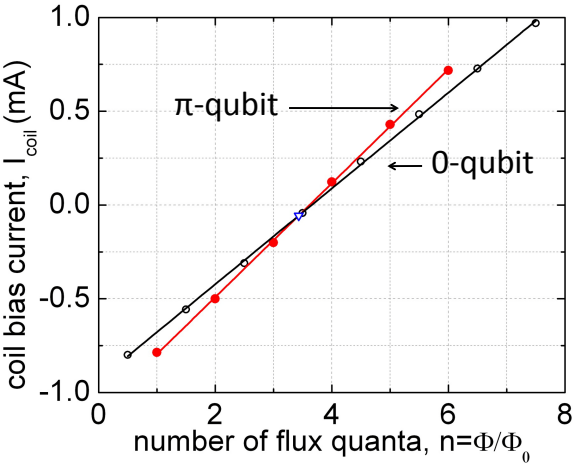

Figure 5.16: The magnetic coil currents vs flux quanta. The horizontal axis is normalized to have the peaks of the π-qubit at integer values of Φ/Φ_0.

the resonator. On the other hand, for the peak family with the smaller amplitude we observe a smaller detuning from the resonator frequency. From the consideration of values of both parameters in

$$\Delta\omega_r = \pm\frac{\tilde{g}^2}{\omega_q - \omega_r}, \tag{5.2}$$

we can see, that interplay of these two parameters and other unknown factors defines the response amplitude in our measurements.

There is also a secondary sign, which can help us in developing the understanding of the pattern. In the year 2006 Kato and Nakamura published a paper, where it was described that the

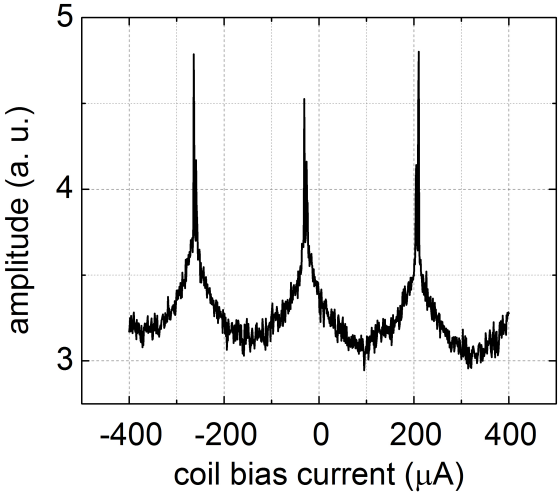

Figure 5.17: Example of the field response of the Al-based flux qubit. The data are obtained for the sample #1, resonator #3 fixed at the resonance frequency of f_r=10.886 GHz.

presence of the ferromagnetic layer decreases the coherence time of the qubit [35]. On our spectroscopy plots we do indeed observe a wider spectroscopy line for one of the qubits (see Figs. 5.12, 5.13).

In order to bring the above discussion in consequence with the intersection method, we should suppose, that we have so bad magnetic shielding in the system, that the offset in field response measurements can exceed a half of a flux quanta. In principle, it is not impossible, because even for Al-based flux qubit without any SFS mesa the measured shift was quite significant, see Fig. 5.17.

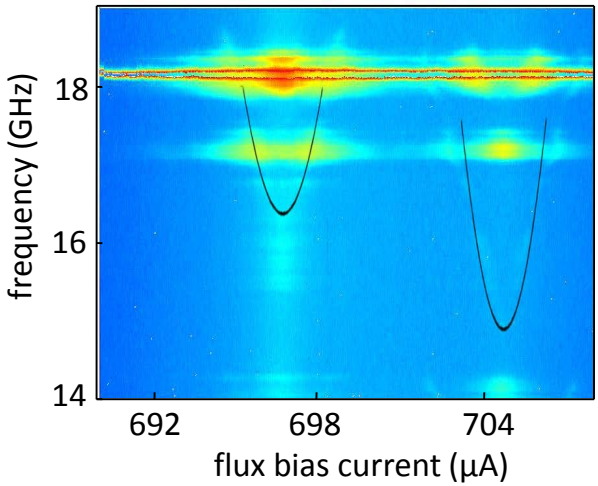

Figure 5.18: Amplitude of microwave probe tone transmission through the feed line, coupled to the $\lambda/4$ resonator with two hybrid qubits with and without SFS mesa, sample #2, resonator #1 with f_r=10.253 GHz.

At the coil bias current around $I_{coil} = 700\ \mu$A two peaks on Fig. 5.15 overlap, giving a wonderful opportunity to perform spectroscopy of both qubits simultaneously, see Fig. 5.18.

We can clearly see the difference in qubit gaps being extracted as 16.3 and 14.9 GHz. The spectroscopy line of both qubits is smeared what we attribute to the extremely low quality factor of the resonator. The resonance at about 18.1 GHz is assigned to the internal sample holder resonance and was subtracted from data in order to increase the plot contrast.

Table 5.6: Characteristics of hybrid qubits, sample #2.

device	1a	1b	2	3	5	6	unit
type	π	0	π	π	0	0	
period	324	274	285	418	457	451	μA
$M_{q,coil}$	6.4	7.6	7.3	4.95	4.5	4.6	pH
α-factor	69	69.4	69.8	70.2	70.6	71	%
$\Delta_{estimated}$	3.5	3.2	3.0	2.7	2.5	2.3	GHz
$\Delta_{measured}$	16.3	14.9	13.3				GHz

In Tab. 5.6 the parameters of sample #2 are summarized. Two qubits, with and without SFS mesa near the first resonator are marked in the table as 1a and 1b.

One can observe a significant difference in the periods qubits with and without SFS mesa near the first resonator (of about $I_{coil} = 50$ μA of the coil bias current) which one could refer to the difference in their inductances, as mentioned above. Also for this sample we see, that measured and estimated qubit gaps decrease with increasing of α-factor of the small Al Josephson junction, as predicted by theory in Sec. 2.3.2.

Measurements of sample #3

The resonators of the sample #3 showed much better quality factors, in spite of a big number of fabrication cycles performed on this sample. The summary on them is represented in Tab. 5.8.

The qubits were fabricated aiming the same values of critical currents and capacitances as for sample #2. As a re-

Table 5.7: Characteristics of resonators for sample #3.

Resonator	Resonance frequency	Quality factor
1	10.253 GHz	20560
2	10.435 GHz	10435
3	10.617 GHz	15167
4	11.245 GHz	22491
5	11.461 GHz	22921
6	11.655 GHz	1665
7	11.748 GHz	783

sult, we do suppose the junction parameters to be $I_c = 1 \pm 0.3$ μA, $C = 4.4 \pm 0.9$ fF, $E_J = (3.3 \pm 0.9) \cdot 10^{-22}$ J and $E_c = (2.9 \pm 0.6) \cdot 10^{-24}$ J. In this case, we measured a nice spectroscopy plot of the hybrid 0-qubit on the fifth resonator (see Fig. 5.19) and one from the hybrid flux qubit near the first resonator (see Fig. 5.20).

In this case, the qubit near the fifth resonator had the mismatch between the designed α=69 % and fitted α=59.6 % equal to 9.4 %. In addition, we observed the strange resonance exactly at the symmetry point of the qubit spectra, what prevented us from measuring Rabi oscillations on this qubit. This parasitic resonance can't be explained by the sample holder modes, as we do not see it during the measurements of the hybrid qubits on the sample #2.

At around 16.3 GHz (showed by the black dashed line in Fig. 5.19) we observe a kind of avoided level crossing pattern, which can be attributed to the interaction of the flux qubit with an atomic two-level tunneling system (TLS), thoroughly

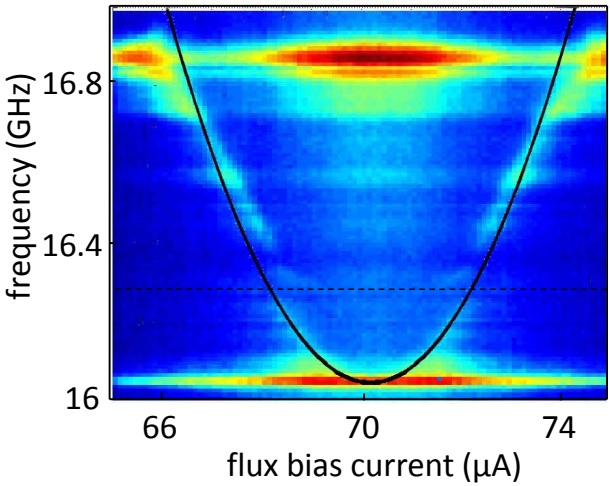

Figure 5.19: Amplitude of microwave probe tone transmission through the feed line, coupled to the $\lambda/4$ resonator, f_r=11.461 GHz, with the hybrid 0-qubit, sample #3, resonator #5.

investigated for phase qubits in [70, 71] and [72]. The atomic-scale defects named TLS in Josephson tunnel barriers can have different fixed resonance frequencies. The coupling between the qubit and TLSs leads to characteristic anticrossings in qubit spectroscopy, what has been shown in [70] and what we most probably see in Fig. 5.19.

For the hybrid qubit, situated near the first resonator, we surprisingly do not observe any mismatch in the designed and fitted α-factor. However, the contrast of the spectroscopy line is very bad, mostly giving just a contour of the hyperbola. The numerous resonances have unexplained nature, also not being observed for the previously measured hybrid qubits.

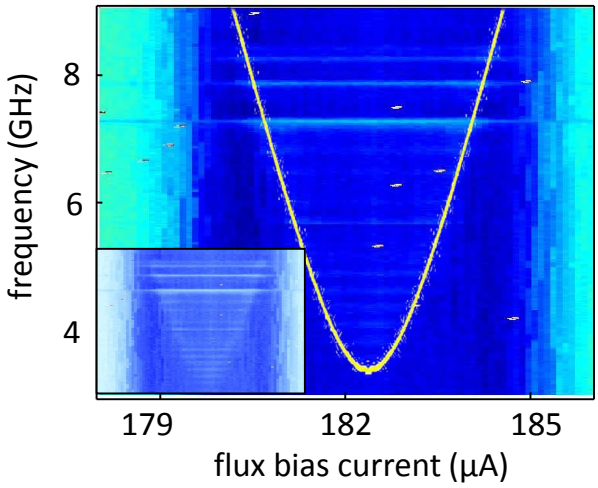

Figure 5.20: An amplitude of a microwave probe tone transmitted through the feed line, coupled to the $\lambda/4$ resonator, f_r=10.253 GHz, sample #3, resonator #1. The inset shows the raw spectrum data.

For this sample, a field response of both qubits situated near the first resonator was measured as well (see Fig. 5.21).

The period of one of the peak families is again 18 % larger than of the other one, what can support the idea of the larger sensitivity of the flux qubit with the SFS mesa to the external flux bias due to the additional inductance. The peaks of one family are doubled, showing that the qubit gap is situated lower than the resonator frequency, what was actually proven by spectroscopy measurements (see Fig. 5.20 and Tab. 5.8). The other pattern consists of single peaks, therefore the second qubit should be situated above the resonator frequency. This fact also brings us to the conclusion, that three times amplitude

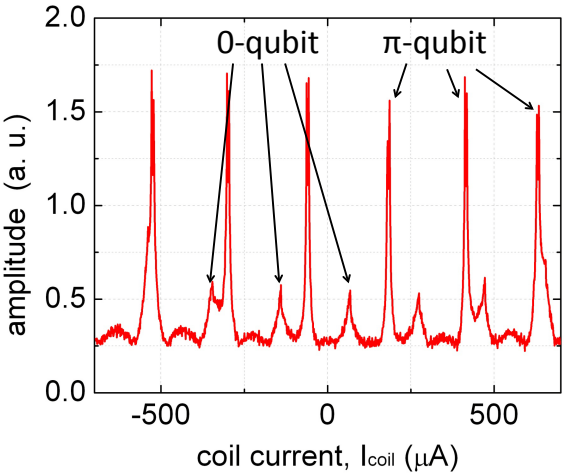

Figure 5.21: Amplitude response of a probe signal through the feed line at a fixed frequency of the $\lambda/4$ resonator $\omega = \omega_r = 10.253$ GHz, sample #3, resonator #1.

difference arises from the different detuning of qubits from the resonator.

For this sample as well we have plotted the positions of peaks as a function of magnetic flux (see Fig. 5.22).

In this case we see, that the intersection point is situated between the peaks of both qubits. After an estimation of the errors we obtained the position of the crossing point $n_c = 2,42 \pm 0.13\ \Phi_0$ having an offset from the peaks of both qubits by $\Delta\Phi^\pi = 0.421 \pm 0.13$. We believe, that in this case we observe two 0-qubits. We explain the transition of π- to 0-junction by too many fabrication cycles with baking of the sample up to 155 °C. It is also known that some samples showed that SFS

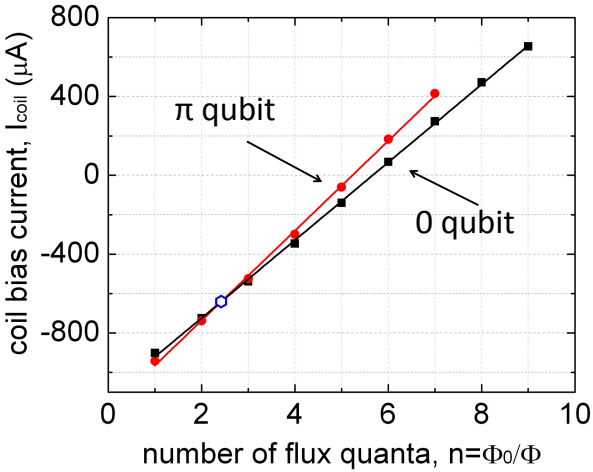

Figure 5.22: The magnetic coil currents vs flux quanta. The horizontal axis is normalized to have the peaks of the π-qubit at integer values of Φ/Φ_0, sample #3, resonator #1.

junctions can have a short due to technological imperfection thus providing no π-junction behavior. This could also be an option why we do not observe a π-shift for the sample #3.

5.5 Conclusion

In conclusion, we developed a fabrication process which allows to create a superconducting interface between Nb and Al/AlO_x/Al Josephson junctions. The process features precooling and Ar etching procedures in-situ before deposition of Josephson junctions using a standard double-angle shadow evaporation. This process can also be implemented for more

Table 5.8: Characteristics of hybrid qubits sample #3.

device	1a	1b	2	3	5	6	unit
type	π	0	π	π	0	0	
period	233	199	201	9.5-40[1]	506		μA
$M_{q,coil}$	8.9	10.4	10.3	51.7	2.4		pH
α-factor	69	69.4	69.8	70.2	70.6	71	%
$\Delta_{estimated}$	3.5	3.2	3.0	2.7	2.5	2.3	GHz
$\Delta_{measured}$	3.5				16.2		GHz

1. On the photo there was found a defect of the qubit near the third resonator.

complex Nb/Al qubit circuits. Hybrid Al/Nb flux qubits containing π-junctions were fabricated using the developed approach.

We measured field response of ten hybrid flux qubits with and without SFS mesas and performed microwave spectroscopy of five of them. For two samples, #2 and #3, we observed the field response of two flux qubits (one with and another without SFS mesa) coupled to the same $\lambda/4$ resonator. For the sample #2, the magnetic field shift between two periodic qubit oscillation patterns measured at mK temperatures indicates the expected π-junction phase bias in one of the flux qubit loops. For the sample #3, we didn't observe any phase biasing presumably due to a large number of technological cycles, which may have caused the $\pi \rightarrow 0$-junction transition by annealing. The reported approach can be used for implementing a variety of hybrid Nb/Al superconducting quantum circuits.

6 Conclusion and Outlook

This thesis presents fabrication and measurements of hybrid Al/Nb flux qubits with SFS π-junctions. Such a qubit type is a complex circuit, one part of which is a Nb wire containing a π-junction, made by optical lithography and DC magnetron sputtering. The other qubit part is aluminum with three Josephson junctions, fabricated using electron-beam lithography and double-angle evaporation. These two parts are made individually and need to be combined. Aluminum two-angle evaporation is performed as the last step in a separate setup, unavoidably exposing pre-fabricated Nb structures to air under which unwanted natural oxide NbO_x is formed on the Nb surface. The challenge we faced was to develop a fabrication procedure combining the two technologies to achieve a transparent Nb/Al contact in hybrid flux qubit rings. This goal was successfully achieved. The thesis gives a detailed description of an Ar beam etching procedure preserving MMA/PMMA resist stack as well as a Ge hard mask technique.

Using the employed approach, hybrid Nb/Al Josephson junctions and flux qubits with and without π-junctions were fabricated. The JJs were characterized at 300 mK in a four-point measurement scheme yielding the targeted design parameters for flux qubits, such as critical current, α-factor, capacitance, etc.

Hybrid flux qubits were fabricated near $\lambda/4$ resonators, which, in turn, were capacitively coupled to the transmission line. The detailed design of hybrid structures is described in Chap. 4. The qubit measurements were performed in the dispersive regime. In this regime, the qubit couples inductively to the resonator, causing a shift of its resonance frequency depending on the qubit quantum state.

Two flux qubits, one with and another without a π-shifter, were fabricated near the shorted end of one of the resonators. We measured the dispersive magnetic field response of these two qubits, observing a magnetic flux $\Phi_0/2$ shift between them attributed to the π-junction. We also took spectroscopy data of hybrid π- and 0-qubits, observing the difference in spectral line-width between them.

One of unsolved problems in the reported measurements remained very low quality factors of superconducting resonators. Future improvements of the design should include the substitution of the Nb resonator material with aluminum, in order to increase the resonator quality factor. This improvement might give a possibility to directly measure the coherence times of the hybrid flux qubits.

Zusammenfassung und Ausblick

In vorliegender Dissertation wurden die Fabrikation und Messungen an hybriden Al/Nb Flussqubits mit SFS π-Kontakten vorgestellt. Solch ein Qubit-Typ ist eine komplexe Schaltung. Ein Teil davon besteht aus einem Nb-Draht, der einen π-Kontakt enthält und mit optischer Lithographie und dem DC Magnetron Kathodenzerstäubungsverfahren hergestellt ist. Der andere Teil des Qubits besteht aus Aluminium und enthält drei Josephson-Kontakte, hergestellt unter der Verwendung von Elektronenstrahllithographie und eines Zweiwinkelverdampfungsverfahrens. Diese beiden Teile werden getrennt voneinander hergestellt und müssen kombiniert werden. Die Aluminium-Zweiwinkelaufdampfung ist der letzte Prozessschritt welcher in einer separaten Anlage stattfindet. Dabei werden zuvor strukturierte Nb-Strukturen unvermeidlich der Luft ausgesetzt, wobei sich an deren Oberfläche unerwünschtes natürliches NbO_x bildet. Eine der Herausforderung, die es zu meistern galt, war die Entwicklung eines Herstellungsprozesses, welcher die beiden Technologien verbindet, um einen elektronisch transparenten Nb/Al-Kontakt in hybriden Flussqubit-Ringen zu erzielen. Dieses Ziel wurde erfolgreich erreicht. Die Dissertation liefert eine detaillierte Beschreibung des Ätzprozesses mit einem

Ar-Strahl, welcher eine Anordnung von MMA/PMMA-Lacken chemisch erhält, sowie einer Ge-Hartmaskentechnologie.

Unter Verwendung dieses Prozesses wurden hybride Josephson-Kontakte aus Nb/Al mit und ohne π-Kontakte hergestellt. Die Josephson-Kontakte wurden bei 300 mK mit einer Vierpunkt-Messanordnung charakterisiert, womit die angestrebten Designwerte für die Flussqubits, wie kritischer Strom, α-Faktor, Kapazität, usw., bestätigt wurden. Die hybriden Flussqubits wurden in der Nachbarschaft von $\lambda/4$-Resonatoren angeordnet, welche wiederum kapazitiv an eine Transmissionline gekoppelt sind. Das Design der hybriden Strukturen ist in Kapitel 4 beschrieben. Die Qubit-Messungen wurden im dispersiven Regime durchgeführt. In diesem Regime koppelt das Qubit induktiv an den Resonator und verursacht eine Verschiebung dessen Resonanzfrequenz, abhängig von dem Quantenzustand des Qubits.

Zwei Flussqubits, eines mit und eines ohne π-Phasenschieber, wurden in der Nähe des kurzgeschlossenen Endes eines der beiden Resonatoren angeordnet. Das dispersive Verhalten bei Anlegen und Veränderung eines magnetischen Feldes dieser beiden Qubits wurde gemessen, wobei sich eine relative Verschiebung des magnetischen Flusses um $\Phi_0/2$ beobachten liess. Dies wurde dem π-Kontakt zugeschrieben. Ausserdem wurden Spektroskopiedaten von hybriden π- und 0-Qubits aufgenommen, wobei man den Unterschied ihrer spektralen Linienbreiten beobachten konnte.

Eines der ungelösten Probleme in den dargelegten Messungen ist die sehr niedere Güte der supraleitenden Resonatoren. Bei zukünftigen Verbesserungen des Designs sollte Nb als Resonatormaterial durch Aluminium ersetzt werden um die Güte des Resonators zu erhöhen. Diese Verbesserung könnte es er-

möglichen die Kohärenzzeiten der hybriden Flussqubits direkt zu messen.

7 List of publications

1. K. G. Fedorov, A. V. Shcherbakova, R. Schaefer and A. V. Ustinov. Josephson vortex coupled to the flux qubit. *Appl. Phys. Lett.* **102** 132602, 2013.

2. K. G. Fedorov, Anastasia V. Shcherbakova, Michael J. Wolf, Detlef Beckmann, and Alexey V. Ustinov. Fluxon readout of a superconducting qubit. *Phys. Rev. Lett.* **112** 160502, 2014.

3. A. V. Shcherbakova, K. G. Fedorov, K. V. Shulga, V. V. Ryazanov, V. V. Bolginov, V. A. Oboznov, S. V. Egorov, V. O. Shkolnikov, M. Wolf, D. Beckmann and A. V. Ustinov. Fabrication and measurements of hybrid Nb/Al Josephson junctions and flux qubits with π-shifters. *ArXiv:* 1405.0373v1.

Bibliography

[1] E. Knill, R. Laflamme, and G. J. Milburn. A scheme for efficient quantum computation with linear optics. *Nature*, 409(6816):46–52, Jan 2001.

[2] Daniel Loss and David P. DiVincenzo. Quantum computation with quantum dots. *Phys. Rev. A*, 57(1):120–126, Jan 1998.

[3] B. E. Kane. A silicon-based nuclear spin quantum computer. *Nature*, 393(6681):133–137, May 1998.

[4] J. I. Cirac and P. Zoller. Quantum Computations with Cold Trapped Ions. *Phys. Rev. Lett.*, 74(20):4091–4094, May 1995.

[5] L. Childress, M. V. Gurudev Dutt, J. M. Taylor, A. S. Zibrov, F. Jelezko, J. Wrachtrup, P. R. Hemmer, and M. D. Lukin. Coherent Dynamics of Coupled Electron and Nuclear Spin Qubits in Diamond. *Science*, 314(5797):281–285, 2006.

[6] J. Clarke and F. K. Wilhelm. Superconducting quantum bits. *Nature*, 459:1031–1042, 2008.

[7] J. Q. You and F. Nori. Atomic physics and quantum optics using superconducting circuits. *Nature*, 474:589–597, 2011.

[8] A. Lupascu, P. Bertet, C. J. P. Driessen, M. Harmans, and J. E. Mooij. One- and two-photon spectroscopy of a flux qubit coupled to a microscopic defect. *Phys. Rev. B*, 80:172506, 2011.

[9] John Martinis. Superconducting phase qubit. *Quantum Inf. Process*, 8:81, 2009.

[10] J. C. Lee, W. D. Oliver, K. K. Berggren, and Orlando T. P. Nonlinear resonant behavior of a dispersive readout circuit for a superconducting flux qubit. *Phys. Rev. B*, 75:144505, 2007.

[11] J. Lisenfeld, O. Lukashenko, M. Ansmann, J. M. Martinis, and Ustinov A. V. Temperature dependence of coherent oscillations in josephson phase qubits. *Phys. Rev. Lett.*, 99:170504, 2007.

[12] E. Hoskinson, F. Lecocq, N. Didier, A. Fay, F. W. J. Hekking, W. Guichard, O. Buisson, R. Dolata, B. Mackrodt, and A. B. Zorin. Quantum dynamics in a camelback potential of a dc SQUID. *Phys. Rev. Lett.*, 102:097004, 2009.

[13] M. Jerger, S. Poletto, P. Macha, U. Hb̈ner, A. Lukashenko, E. Il'ichev, and A. V. Ustinov. Readout of a qubit array via a single transmission line. *EPL (Europhysics Letters)*, 96(4):40012, 2011.

[14] L. B. Ioffe, V. B. Geschkenbein, M. V. Feigelman, A. L. Feuchere, and G. Blaetter. Environmentally decoupled sds wave Josephson junctions for quantum computing. *Nature*, 395:679–681, 1999.

[15] Gianni Blatter, Vadim B. Geshkenbein, and Lev B. Ioffe. Design aspects of superconducting-phase quantum bits. *Phys. Rev. B*, 63:174511, Apr 2001.

[16] V. A. Oboznov, V. V. Bol'ginov, A. K. Feofanov, V. V. Ryazanov, and A. I. Buzdin. Thickness Dependence of the Josephson Ground States of Superconductor-Ferromagnet-Superconductor Junctions. *Phys. Rev. Lett.*, 96:197003, May 2006.

[17] S.M. Frolov, M. J. A. Stoutimore, T.A. Crane, D.J. Van Harlingen, V.A. Oboznov, V.V. Ryazanov, A. Ruosi, C. Granata, and M. Russo. Imaging spontaneous currents in superconducting arrays of π-junctions. *Nat. Phys.*, 4:32, Nov 2007.

[18] Ustinov A. V. and Kaplunenko V. K. Rapid single-flux quantum logic using π-shifters. *J. App. Phys.*, 94:5405, Sep 2003.

[19] A. K. Feofanov, V. A. Oboznov, V. V. Bolginov, J. Lisenfeld, S. Poletto, V. V. Ryazanov, A. N. Rassolenko, M. Khabipov, D. Balashov, A. B. Zorin, P. N. Dmitriev, V. P. Koshelets, and Ustinov A. V. Implementation of superconductor/ferromagnet/superconductor π-shifters in superconducting digital and quantum circuits. *Nat. Phys.*, 6:593, Jun 2010.

[20] V.V. Schmidt. *The Physics of Superconductors: Introduction to Fundamentals and Applications*. Springer, 2010.

[21] A. Einstein. Kuratoriumssitzung der Physikalisch-Technischen Reichsanstalt Berlin Charlottenburg:

"Von besonderem Interesse ist die Frage, ob die Verbindungsstelle zwischen zwei Supraleitern auch supraleitend wird.", March 1926.

[22] B. D. Josephson. Possible new effects in superconductive tunnelling. *Physics Letters*, 1(7):251 – 253, 1962.

[23] B. D. Josephson. Coupled Superconductors. *Rev. Mod. Phys.*, 36:216–220, Jan 1964.

[24] P. W. Anderson and J. M. Rowell. Probable Observation of the Josephson Superconducting Tunneling Effect. *Phys. Rev. Lett.*, 10:230–232, Mar 1963.

[25] T. P. Orlando, J. E. Mooij, Lin Tian, Caspar H. van der Wal, L. S. Levitov, Seth Lloyd, and J. J. Mazo. Superconducting persistent-current qubit. *Phys. Rev. B*, 60:15398–15413, Dec 1999.

[26] W. Meissner and Ochsenfeld R. Ein neuer Effekt bei Eintritt der Supraleitfähigkeit. *Naturwissenschaften*, 21:787–788, November 1933.

[27] David P. DiVincenzo. The physical implementation of quantum computation. *http://arxiv.org/pdf/Quant-Ph/0002077.pdf*, pages 1–9, 2008.

[28] K. G. Fedorov, A. V. Shcherbakova, R. Schaefer, and A. V. Ustinov. Josephson vortex coupled to the flux qubit. *Appl. Phys. Lett.*, 102:132602–132606, 2013.

[29] T. P. Orlando, J. E. Mooij, Lin Tian, Caspar H. van der Wal, L. S. Levitov, Seth Lloyd, and J. J. Mazo. Su-

perconducting persistent-current qubit. *Phys. Rev. B*, 60:15398–15413, Dec 1999.

[30] Milena Grifoni and Peter Hänggi. Driven quantum tunneling. *Physics Reports*, 304:229–354, 1998.

[31] E. A. Demler, G. B. Arnold, and M. R. Beasley. Superconducting proximity effects in magnetic metals. *Phys. Rev. B*, 55:15174–15182, Jun 1997.

[32] A. I. Buzdin. Proximity effects in superconductor-ferromagnet heterostructures. *Rev. Mod. Phys.*, 77:935–976, Sep 2005.

[33] L. N. Bulaevskii, V. V. Kuzii, and A. A. Sobyanin. Superconducting system with weak coupling to the current in the ground state. *JETP Lett.*, 25:290–294, 1977.

[34] V. V. Ryazanov, V. A. Oboznov, V. V. Bolginov, A. S. Prokofiev, and A. K. Feofanov. Supercurrents through the ferromagnetic. Inversion of the phase in the structures with Josephson π-junctions. *Conferences and symposiums*, 174:795–800, 2004.

[35] T. Kato, A. A. Golubov, and Y. Nakamura. Decoherence in a superconducting flux qubit with a π-junction. *Phys. Rev. B*, 76:172502, Nov 2007.

[36] A. N. Omeljanchouk, S. N. Shevchenko, Y. S. Greenberd, O. Astafiev, and E. Ilichev. Quantum behavior of a flux qubit coupled to a resonator. *Low Temp. Phys*, 36:893–901, 2010.

[37] A. Blais, R.-S. Huang, A. Wallraff, S. M. Girvin, and R. J. Schoelkopf. Cavity quantum electrodynamics for superconducting electrical circuits: An architecture for quantum computation. *Phys. Rev. A*, 69:062320, Jun 2004.

[38] L. D. Landau and E. M. Lifshitz. *Quantum mechanics : non-relativistic theory.* Pergamon Press, 1994.

[39] Floor Paaw. *Superconducting Flux Qubits: Quantum chains and tunable qubits.* PhD thesis, Delft, May 2009.

[40] Y. Makhlin, G. Schön, and Shnirman A. Quantum-state engineering with Josephson junction devices. *Rev. Mod. Phys.*, 73:357–397, 2001.

[41] J. Plantenberg. *Coupled superconductive flux qubits.* PhD thesis, Delft, May 2007.

[42] G. Ithier, E. Collin, P. Joyez, P. J. Meeson, D. Vion, D. Esteve, F. Chiarello, A. Shnirman, Y. Makhlin, J. Schriefl, and G. Schön. Decoherence in a superconducting quantum bit circuit. *Phys. Rev. B*, 72:134519, Oct 2005.

[43] V. A. Oboznov, V. V. Bolginov, A. N. Rossolenko, and V. V. Ryazanov. *to be published*, 2014.

[44] http://www.britannica.com/ebchecked/topic/1551203/polymethyl-methacrylate-pmma.

[45] URL: www.microchem.com. MicroChem Corp.

[46] URL: www.werkstoffanalytik.de. ZWL.

[47] URL: www.raith.com. Raith GmbH.

[48] M Von Schickfus and S. Hunklinger. Saturation of the dielectric absorption of vitreous silica at low temperatures. *Phys. Lett. A*, 64(1):144 – 146, 1977.

[49] D. S. Wisbey, J. Gao, M. R. Vissers, F. C. S. da Silva, J. S. Kline, L. Vale, and D. P. Pappasa. Effect of metal/substrate interfaces on radio-frequency loss in superconducting coplanar waveguides. *J. Appl. Phys.*, 108:093918, 2010.

[50] J. M. Sage, V. Bolkhovsky, W. D. Oliver, B. Turek, and P. B. Welander. Study of loss in superconducting coplanar waveguide resonators.

[51] J. M. Martinis, K. B. Cooper, R. McDermott, M. Steffen, M. Ansmann, K. D. Osborn, K. Cicak, S. Oh, D. P. Pappas, R. W. Simmonds, and C. C. Yu. Decoherence in Josephson Qubits from Dielectric Loss. *Phys. Rev. Lett.*, 95:210503, 2005.

[52] A. D. O'Connell, M. Ansmann, R. C. Bialczak, M. Hofheinz, N. Katz, E. Lucero, C. McKenney, M. Neeley, H. Wang, E. M. Weig, A. N. Cleland, and J. M. Martinis. Microwave dielectric loss at single photon energies and millikelvin temperatures. *J. Appl. Phys.*, 92:112903, 2008.

[53] M. Jerger. *Experiments on Superconducting Qubits Coupled to Resonators*. PhD thesis, Karlsruhe, February 2013.

[54] A. V. Ustinov and V. K. Koplunenko. Rapid single-flux logic using π-shifters. *J. Appl. Lett.*, 94:5405–5408, 2003.

[55] Abrikosov A. A. On the magnetic properties of superconductors of the second group. *JETP*, 32:1442–1452, Dec 1957.

[56] URL: www.anritsu.com. Anritsu Corporation.

[57] L. Capogna and M. G. Blamire. Superconducting proximity effect through high-quality high-conductance tunnel barriers. *Phys. Rev. B*, 53(9):5683–5687, Mar 1996.

[58] H. Sugiyama, A. Yanada, M. Ota, A. Fujimaki, and H. Hayakawa. Characteristics of Nb/Al/Alox/Al/Alox/Nb junctions based on the proximity effect. *Jpn. J. Appl. Phys.*, 36(9A/B):1157–1160, Jul 1997.

[59] S. V. Lotkhov, E. M. Tolkacheva, D. V Balashov, M. I. Khabipov, F.-I. Buchholz, and A. B. Zorin. Low hysteretic behavior of Al/Alo$_x$/Al josephson junctions. *Appl. Phys. Lett.*, 89:132115–132118, 2006.

[60] T. P. Orlando, J. E. Mooij, Lin Tian, Caspar H. van der Wal, L. S. Levitov, and Seth Lloyd. Josephson Persistent-Current Qubit. *Science*, 285:1036, Aug 1999.

[61] F. Hübler, M. J. Wolf, T. Scherer, D. Wang, D. Beckmann, and H. v. Löhneysen. Observation of Andreev bound states at spin-active interfaces. *Phys. Rev. Lett.*, 109:087004, Aug 2012.

[62] Pozar David M. *Microwave Engineering*. John Wiley and Sons, 1998.

[63] A. Khanna and Y. Garault. Determination of loaded, unloaded, and external quality factors of a dielectric resonator coupled to a microstrip line. *Microwave Theory and Techniques, IEEE*, 31:261 – 264, Mar 1983.

[64] T. Yamamoto, K. Inomata, K. Koshino, P.-M. Billangeon, Y. Nakamura, and J. S. Tsai. Superconducting flux qubit capacitively coupled to an lc resonator. *New J. Phys.*, 16:015017, 2014.

[65] Y. S. Shimazu, M. Akashi, and N. Kamura. Observation of higher-order sideband transitions and first-order sideband rabi oscillations in a superconducting flux qubit coupled to a SQUID plasma mode. *J. Phys. S. Japan*, 82:074710, 2013.

[66] K. G. Fedorov. *Fluxon readout for superconducting flux qubits*. PhD thesis, Karlsruhe, April 2013.

[67] K. G. Fedorov, A. V. Shcherbakova, M. J. Wolf, D. Beckmann, and A. V. Ustinov. Fluxon readout of a superconducting qubit. *Phys. Rev. Lett.*, 112:160502, 2014.

[68] C. Song, T. W. Heitmann, M. P. DeFeo, K. Yu, R. McDermott, M. Neeley, John M. Martinis, and B. L. T. Plourde. Microwave response of vortices in superconducting thin films of Re and Al. *Phys. Rev. B*, 79:174512, May 2009.

[69] A. V. Shcherbakova, K. G. Fedorov, K. V. Shulga, V. V. Ryazanov, V. V. Bolginov, V. A. Oboznov, S. V. Egorov, V. O. Shkolnikov, M. J. Wolf, D. Beckmann, and A. V. Ustinov. Fabrication and measurements of hybrid Nb/Al

josephson junctions and flux qubits with π-shifters. *to be published.*

[70] G. J. Grabovskij, P. Bushev, J. H. Cole, C. Mueller, J. Lisenfeld, O. Lukashenko, and A. V. Ustinov. Entangling microscopic defects via a macroscopic quantum shuttle. *New J. Phys.*, 13:063015, 2011.

[71] G. J. Grabovskij, T. Peichl, J. Lisenfeld, G. Weiss, and A. V. A. Ustinov. Strain tuning of individual atomic tunneling systems detected by a superconducting qubit.

[72] G. Grabovskij. *Investigation of coherent microscopic defects inside the tunneling barrier of a Josephson junction.* PhD thesis, Karlsruhe, June 2013.

Danksagung

First of all I would like to thank professor Alexey V. Ustinov for the given possibility to do a PhD work in his group. He became for me not only a competent and broad-minded partner in scientific discussions, but also an example of impressive group leader, who was always interested in lives of group members. Due to encouragement of my motivation and initiative by giving me the possibility to attend different conferences and scientific schools, my time in his group became really unforgettable, challenging and inspiring.

Professor Georg Weiss was so kind to agree to be my corrector and check the thesis in quite a short time. I will save warm feelings to his friendliness and understanding of the situation.

I am deeply grateful to my husband, Dr. Kirill Fedorov, who became my first supervisor when I came in Karlsruhe. It was an honor to work together with the person, whose sense of purpose gave the possibility to rely on his work in any situation. His moral support in both success and failures can't be over-appreciated.

The support and kind attention of my mentor, Prof. Dr. Alexandr Mirlin, and Dr. Alexandr Dmitriev I felt through all the time of my PhD. I am grateful to them from whole my heart.

I want to thank my colleagues, Dr. Fengbin Song, Prof. Dr. Pavel Bushev, Dr. Tobias Wirth, Dr. Jochan Zimmer, Gerda Fischer, Sebastian Skacel for the nice atmosphere in the group,

and in particularly Susanne Butz, who was always willing to help and supported my self-confidence in this man's world. The presence of Ilia Egorov stimulated a lot of IT discussions, I thank him for advices and help in this area.

Special thanks I would like to address to Dr. Marcus Jerger, Dr. Hannes Rotzinger, Dr. Juergen Lisenfeld, Dr. Grigori Grabovski, Sebastian Probst and Dr. Oleksandr Lucashenko for the fruitful discussions, which widened my knowledge in the area of quantum physics.

I want to thank my collaborators Simone Dehm, Prof. Dr. Ralph Krupke, Dr. Detlef Beckmann, Dr. Michael Wolf and Stefan Kolenda in INT Campus Nord, who were always an example for me in sample fabrication and gave me numerous valuable advices in this area.

We made a good work with my collaborators from Chernogolovka, Dr. Vitaly Bol'ginov, Vlad Shkol'nikov, Sergey Egorov and Prof, Valery Ryazanov, I thank them for making my π-junction project possible.

Our mechanical (directed by Michael Meyer) and electronic (Roland Jehle and Ulrich Opfer) workshops, as well as the liquefying station (Hans-Willi Pensl and Christoph Sürgers) made our hardware work possible and are sent big thanks.

In-between I also thank my dance colleagues from TSC Astoria and dance partner Konstantin Ort, who always rose my mood in difficult moments.

I will be always grateful to Florian Knöll, who supported me a lot during the last half a year of my PhD period.

Finally, I want to thank my family and friends, especially my mother, Natalia Shcherbakova, who always gave me a courage and rose my self-estimate, although being far away in Russia. I will be always grateful for all, what she has given to me.

Hiermit versichere ich die vorliegende Arbeit selbstaendig angefertigt, alle dem Sinn oder Wortlaut nach entnommenen Inhalte anderer Werke an den entsprechenden Stellen unter Angabe der Quellen kenntlich gemacht und keine weiteren Hilfsmittel verwendet zu haben.

Karlsruhe, den .....